SUPPORTING INFORMATION

Tailoring Robust Al-MOF for Trapping C_2H_6 and C_2H_2 towards Efficient C_2H_4 Purification from Quaternary Mixtures

Subhajit Laha, Nimish Dwarkanath, Abhishek Sharma, Darsi Rambabu, Sundaram Balasubramanian, Tapas Kumar Maji*

Chemistry and Physics of Materials Unit, School of Advanced Materials, Jawaharlal Nehru Centre for Advanced Scientific Research, Jakkur, Bangalore-560064, India.

Table of contents

Materials and synthesis

All the reagents and solvents were commercially available and used as provided without further purification. $Al(NO_3)_3 \cdot 9H_2O$ has been obtained from Sigma-Aldrich Chemical Company. 1,4-naphthaleledicarboxylic acid (1,4-H_2NDC) was obtained from Alfa Aeser Chemicals.

1,4-Naphthalenedicarboxylate (0.108 g, 0.5 mmol) and $Al(NO_3)_3 \cdot 9H_2O$ (0.375 g, 1 mmol) were introduced in a 30 mL wide-neck microwave vial, to this H_2O and EtOH (5 mL each) were added, and further sonicated for 10 minutes. After that, the reaction vial was sealed and placed in MONOWAVE 200 (Anton Paar Monowave Series; Serial Number: 81919734; Instrument
Software Version: 4.10.9376.7) microwave reactor. In microwave, the reaction mixture was heated to 150 °C (with a heating rate of 6 °C /min) and held at the same temperature from 5 to 220 minutes for achieving different products with diverse properties by following previous synthetic procedures.[1] The resulting white solid was filtered and washed with water repetitively and finally with ethanol and dried under vacuum. Products are labeled as Al-$MOFM_5$, Al-$MOFM_{15}$, Al-$MOFM_{30}$, Al-$MOFM_{60}$, Al-$MOFM_{120}$ and Al-$MOFM_{220}$ as the respective reaction times are 5, 15, 30, 60 120, and 220 minutes. The PXRD pattern of the resulting MOFs reveals the formation of the pure crystalline phase as indexed with the simulated pattern of the parent framework.

Physical measurements

The powder XRD pattern of the compounds has been recorded by using Cu-Kα radiation (Bruker D8 Discover; 40 kV, 30 mA). The PXRD pattern (Fig. S1) of the resulting MOFs of varied reaction conditions (5, 15, 30, 60, 120, 220 minutes) reveals the formation of the pure crystalline phase of ([Al(OH)(1,4-NDC)]·$2H_2O$) Morphological studies have been carried out using Lica-S440I Field Emission Scanning Electron Microscope (FESEM) by placing samples on a silicon wafer under high vacuum with an accelerating voltage of 100 kV. Thermo gravimetric analysis (TGA) was carried out in N_2 atmosphere (50 $mLmin^{-1}$ flow rate) in the temperature range of 30 to 800 °C with a 5 °C min^{-1} heating rate.

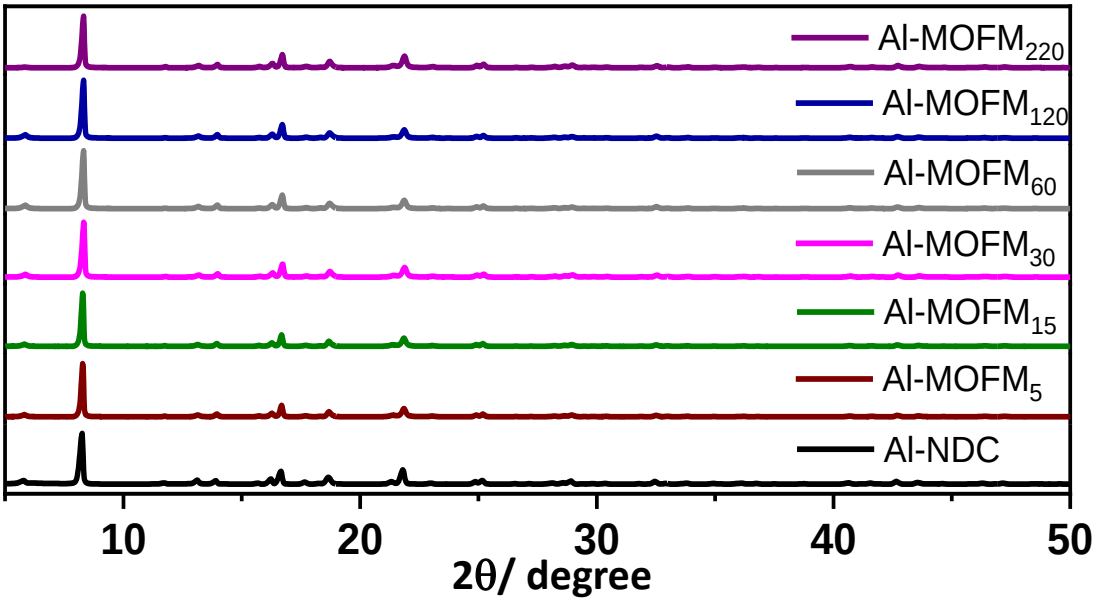

Fig. S1. PXRD patterns of Al-NDC (Al-MOFM$_5$, Al-MOFM$_{15}$, Al-MOFM$_{30}$, Al-MOFM$_{50}$, Al-MOFM$_{120}$ and Al-MOFM$_{220}$) synthesized through microwave reactor by varying reaction time.

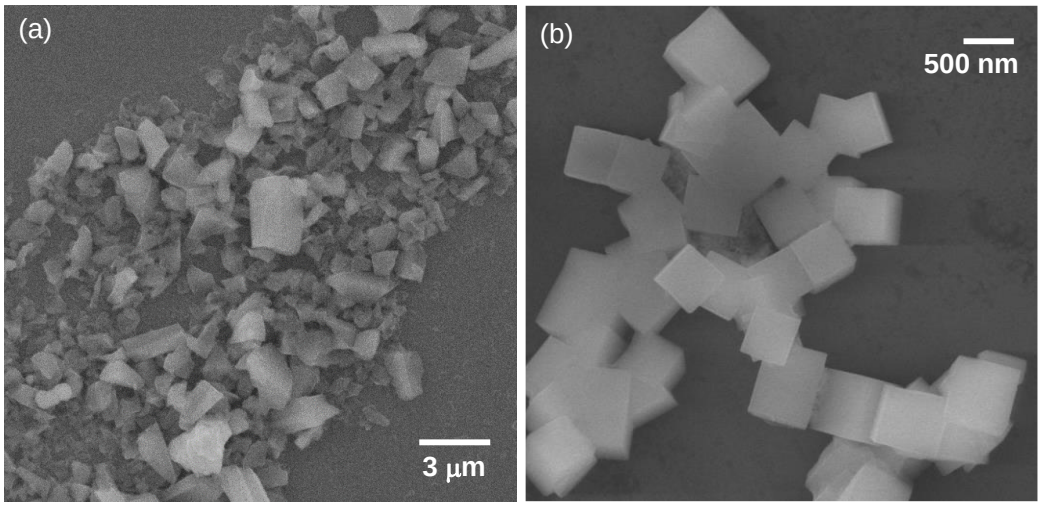

Fig. S2. FESEM images of (a) hydrothermally synthesized non-porous Al-MOF and (b) microwave synthesized tailor-made micro-mesoporous Al-MOFM$_{15}$.

Analysis of gas adsorption isotherms

The adsorption-desorption isotherms of hydrocarbons (CH_4, C_2H_2, C_2H_4 and C_2H_6) and CO_2 Al-MOFM$_{15}$ were measured using QUADRASORB-SI analyzer and AUTOSORB IQ$_2$ instrument at 273 and 293 K, additionally, N_2 isotherm was measured at 77 K. The surface area, pore volume and pore size distribution were calculated from the N_2 adsorption data of the corresponding samples using the ASiQwin software. All the compounds were activated at 150

°C under 1×10^{-1} Pa vacuum for about 16 h prior to isotherm measurements. All the gases used for adsorption measurements are of scientific/research grade with 99.999% purity. Dead volume is measured with helium gas. The surface area was calculated using the Brunauer–Emmett–Teller (BET) theory. The total pore volume is calculated from the amount of vapor adsorbed at a relative pressure close to unity, by assuming that the pores are then filled with a liquid adsorbate. The relation between isotherms derived from the above approaches and the experimental isotherm on a porous solid can be understood by GAI (Generalized Adsorption Isotherm) equation.

$$N\left(\frac{P}{P_0}\right) = \int_{W_{min}}^{W_{max}} N(\frac{P}{P_0}, W) f(W) dW$$

Where, N(P/P_0) = experimental adsorption isotherm data,

W = pore width, N(P/P_0, W) = isotherm on a single pore of width W,

f(W) = pore size distribution function.

The assumption which is reflected from the GAI equation is that the total isotherm consists of a number of individuals "single pore" isotherms multiplied by their relative distribution, f(W), over a range of pore sizes. The set of N(P/P_0, W) isotherms (kernel) for a given system can be obtained by the DFT as indicated above. The pore size distribution can then be derived by solving the GAI equation numerically via a fast non-negative least square algorithm. The ASiQwin software has been used to calculate the pore size distribution using the NLDFT–N_2-carbon equilibrium transition kernel at 77 K based on a slit-pore model. The water adsorption-desorption isotherm was carried out at 293 K under vapor state by using BELSORP-aqua analyzer. All operations were automatic and software controlled.

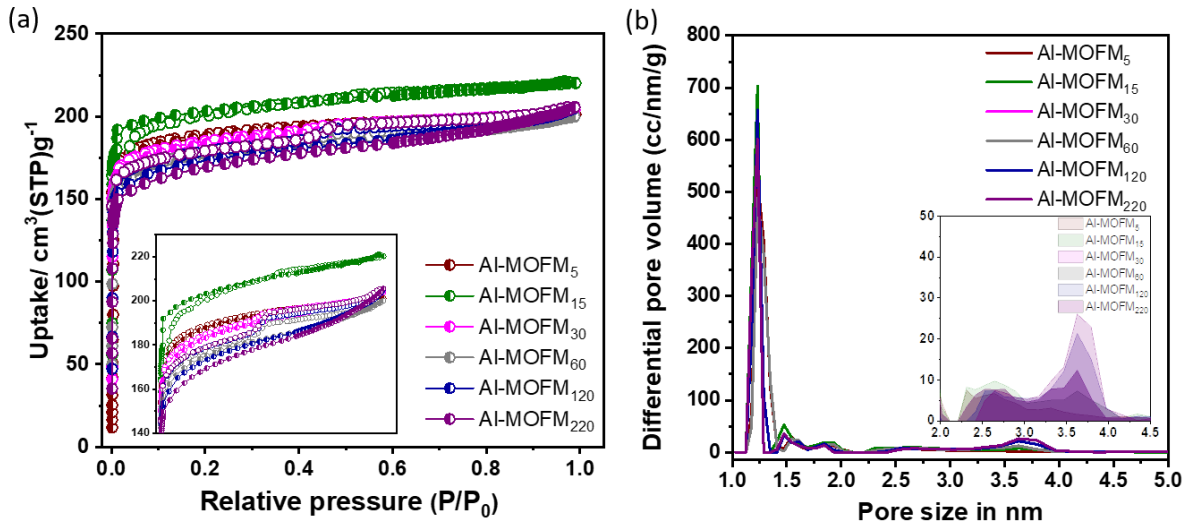

Fig. S3. (a) N_2 adsorption-desorption isotherm of Al-MOFM$_5$, Al-MOFM$_{15}$, Al-MOFM$_{30}$, Al-MOFM$_{60}$, Al-MOFM$_{120}$ and Al-MOFM$_{220}$ at 77 K (*inset*: Focusing on the pressure part of the isotherms) (b) Corresponding pore size distribution plot calculated through non-local density functional theory (NLDFT) method (*inset*: differential pore volume at mesopore region).

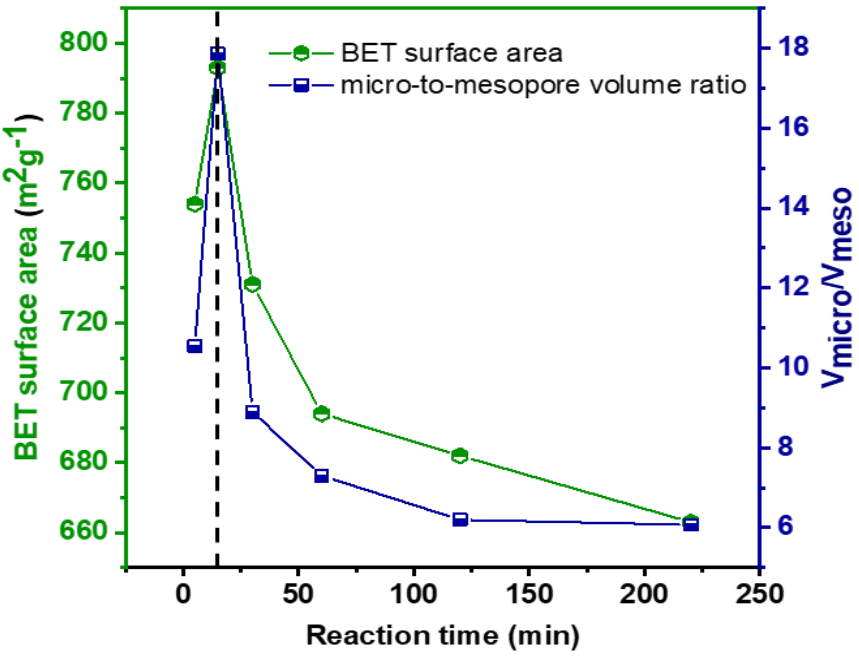

Fig. S4. Comparative BET surface area and micro-to-mesopore volume ratio for Al-MOFM synthesized through microwave reactor under varied reaction time.

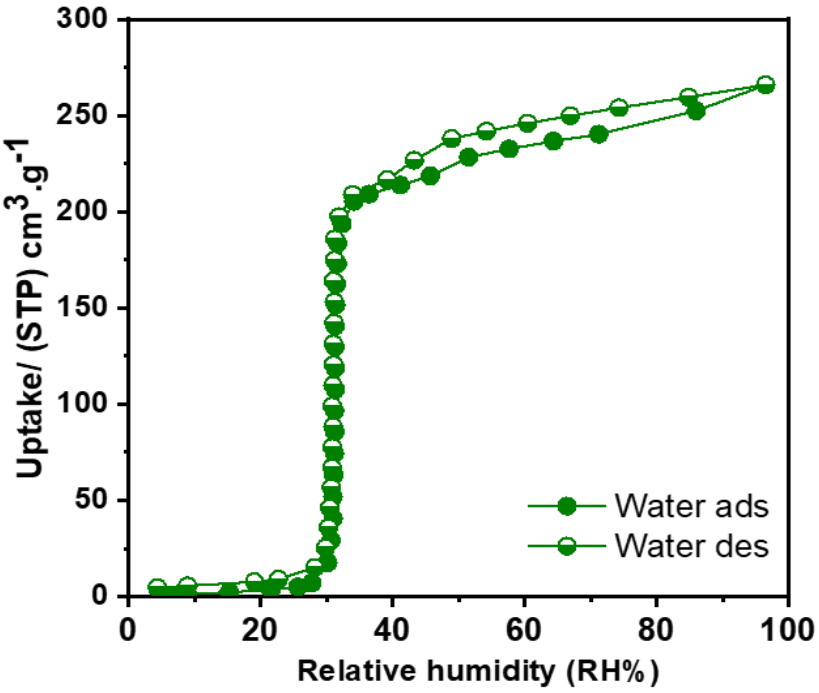

Fig. S5. Water adsorption-desorption isotherm was measured at 293 K for Al-MOFM$_{15}$.

Table S1: Physical parameters of selected gas adsorbates.[2, 3]

	Molecular dimension (Å)			**Kinetic diameter (Å)**	**Boiling point (K)**	**Polarizability×10^{-25} cm^3**	**Quadruple moment×10^{-26} esu cm^2**
	x	**y**	**z**				
CO_2	3.18	3.33	5.36	3.30	194.7	29.11	4.30
CH_4	3.63	3.98	3.98	3.78	111.5	25.93	0
C_2H_2	3.32	3.34	5.76	3.30	188.4	33.3-39.3	--
C_2H_4	3.28	4.18	4.84	4.16	169.4	42.52	1.50
C_2H_6	3.81	4.08	4.82	4.44	184.6	44.3-44.7	0.65

Heat of adsorption

Virial fitting: The virial expression of the following type has been used to simultaneously fit combined single component isotherms at 273, 283 and 293 K.

$$\ln(p) = \ln(A) + \frac{1}{T}\sum_{i=0}^{m} a_i A^i + \sum_{i=0}^{n} b_i A^i \quad \text{(eq. 1)}$$

p is the pressure expressed in torr, A is the amount adsorbed in mmol/g, T is the temperature in K, a_i and b_i are virial coefficients, and m, n represents the number of coefficients required to adequately describe the isotherms (eq. 1). The values of the virial coefficient a_i were taken to calculate the isosteric heat of adsorption using the following expression.[4]

$$Q_{st}(A) = -R\sum_{i=0}^{m} a_i A^i \quad \text{(eq. 2)}$$

Where R is the universal gas constant.

Freundlich-Langmuir (FL) fitting: First, the isotherms measured at different temperatures are fitted independently using the Freundlich-Langmuir isotherm model using the expression,

$$A = \frac{a \cdot b \cdot p^c}{1 + b \cdot p^c} \quad \text{(eq. 3)}$$

Then eq. 3 can be rearranged to obtain the pressure as a function of uptake amount.

$$p(A) = \sqrt[c]{\frac{A}{a \cdot b - A \cdot b}} \quad \text{(eq. 4)}$$

expressions p_1 and p_2 were obtained for FL fits of adsorption isotherms measured at temperatures T_1 and T_2, respectively. Upon applying Clausius-Clapeyron equation, the expression for the isosteric heat of adsorption (Q_{st}) becomes

$$Q_{st}(A) = -R \cdot \ln\left(\frac{p_2}{p_1}\right) \cdot \frac{T_1 \cdot T_2}{T_2 - T_1} \quad \text{(eq. 5)}$$

R is the universal gas constant. Q_{st} was calculated using single-component adsorption isotherms at 273, 283 and 293 K for each of the five gases.

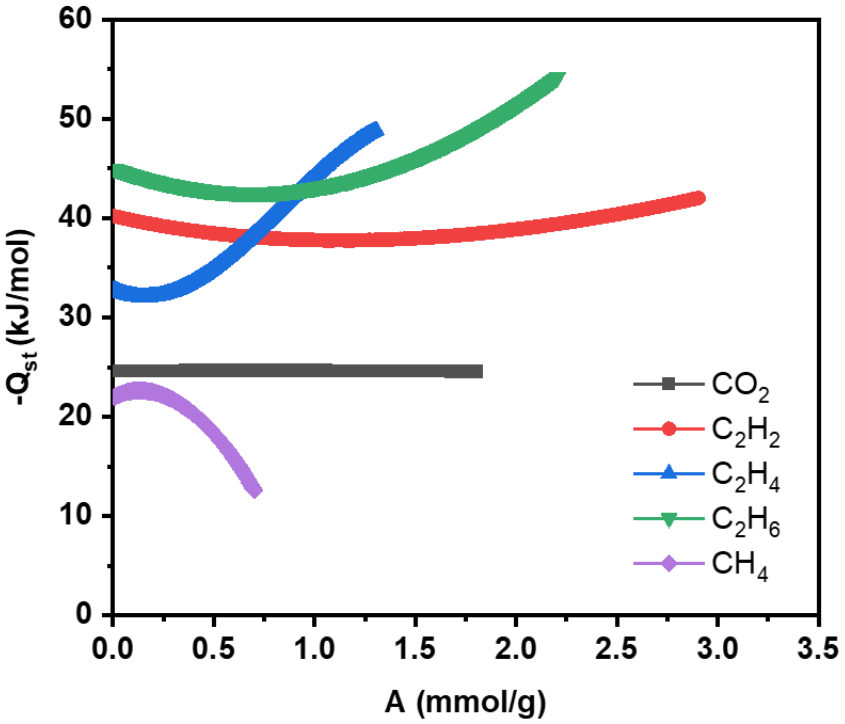

Fig. S6. Isosteric heat of adsorption (Q_{st}) estimated by virial fitting at various loading amounts of CO_2, C_2H_2, C_2H_4, C_2H_6, and CH_4.

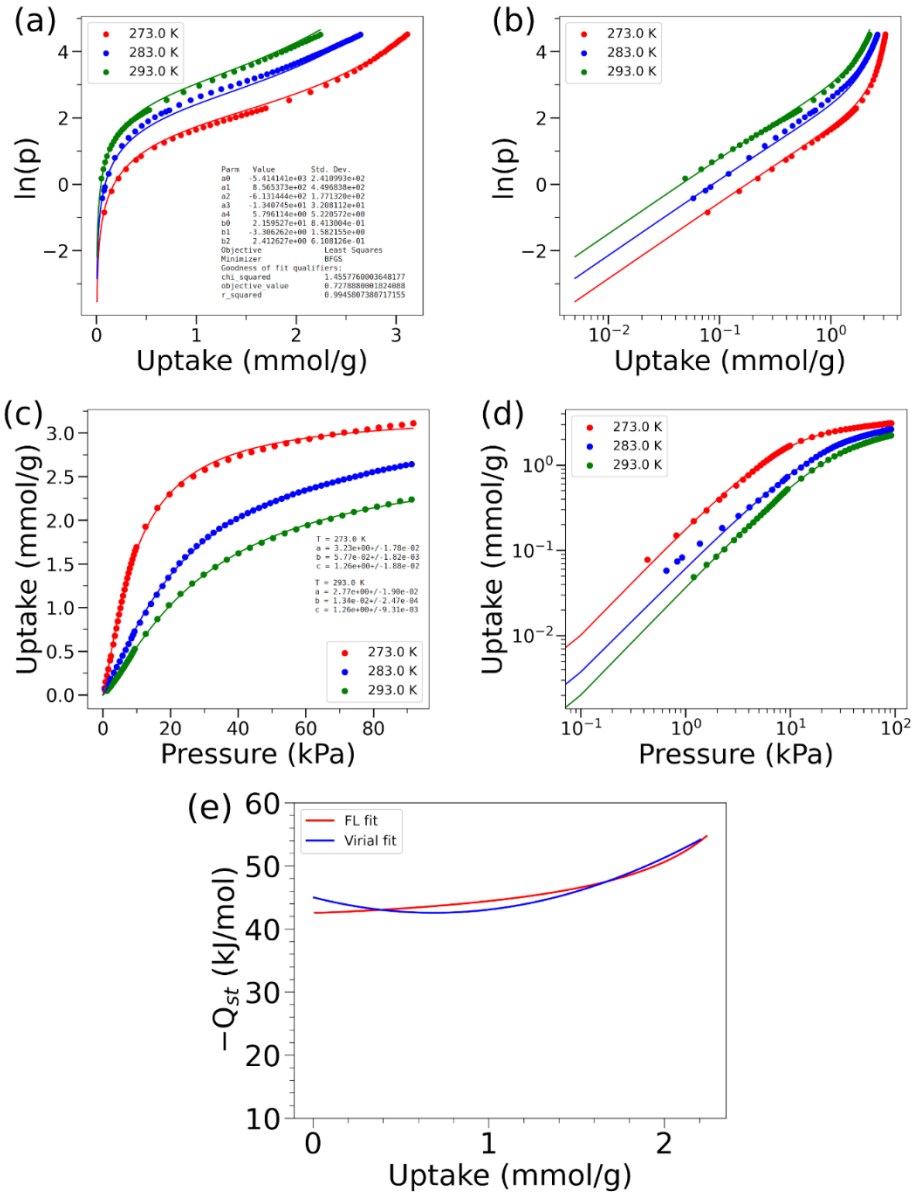

Fig. S7. (a)-(d) Measured adsorption isotherm data (filled circles) and the corresponding (a) & (b) virial and (c) & (d) Freundlich-Langmuir (FL) fits (solid lines) for C_2H_6 in Al-MOFM$_{15}$. (a) and (c) are reproduced with logarithmic scales in (b) and (d), respectively. (e) Isosteric heats of adsorption (Q_{st}) calculated using virial (blue) and FL fits (red), respectively. Q_{st} from Virial fitting were estimated from the fits obtained for 273, 283, and 293 K isotherm data while that from FL-fits were estimated using the 273 and 293 K isotherm fits.

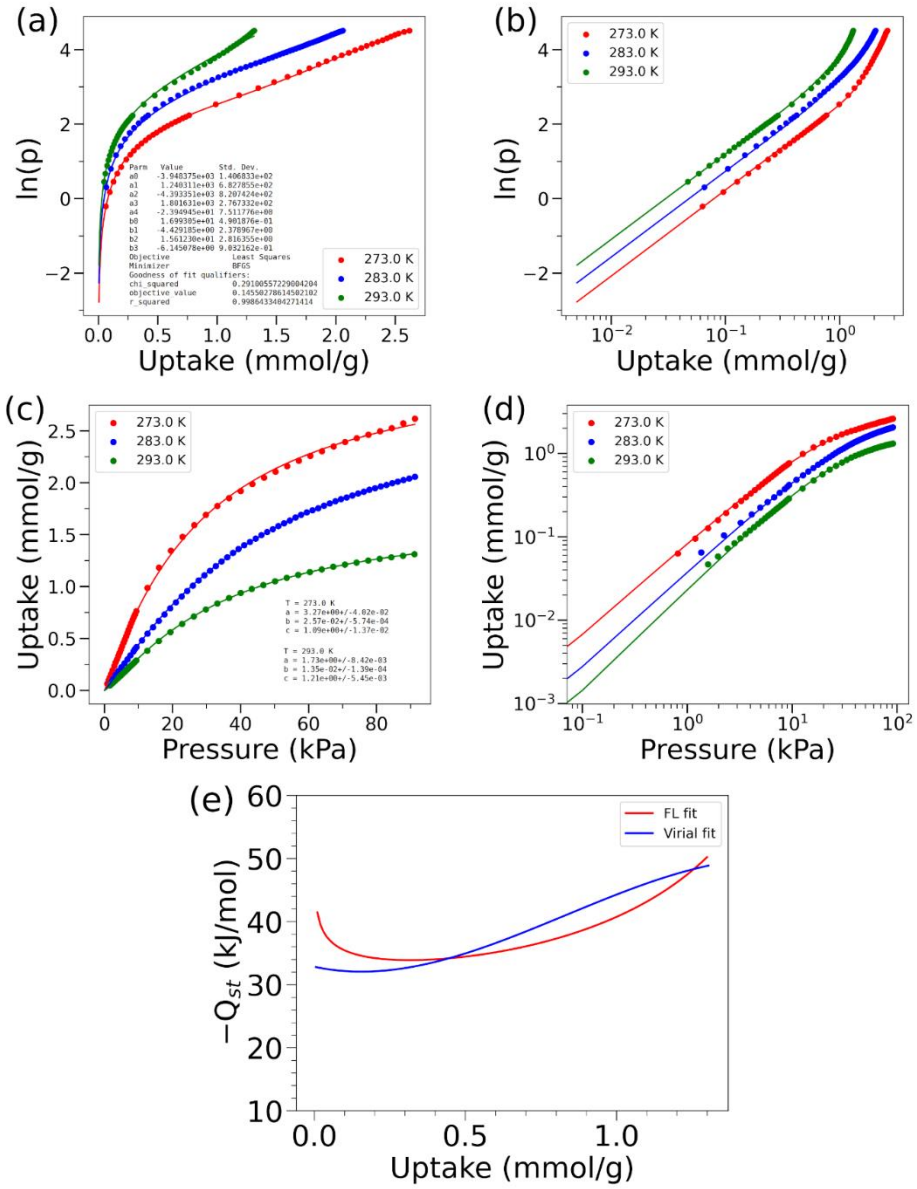

Fig. S8. (a)-(d) Measured adsorption isotherm data (filled circles) and the corresponding (a) & (b) virial and (c) & (d) Freundlich-Langmuir (FL) fits (solid lines) for C_2H_4 in Al-MOFM$_{15}$. (a) and (c) are reproduced with logarithmic scales in (b) and (d), respectively. (e) Isosteric heats of adsorption (Q_{st}) calculated using virial (blue) and FL fits (red), respectively. Q_{st} from virial fitting were estimated from the fits obtained for 273, 283, and 293 K isotherm data while that from FL-fits were estimated using the 273 and 293 K isotherm fits.

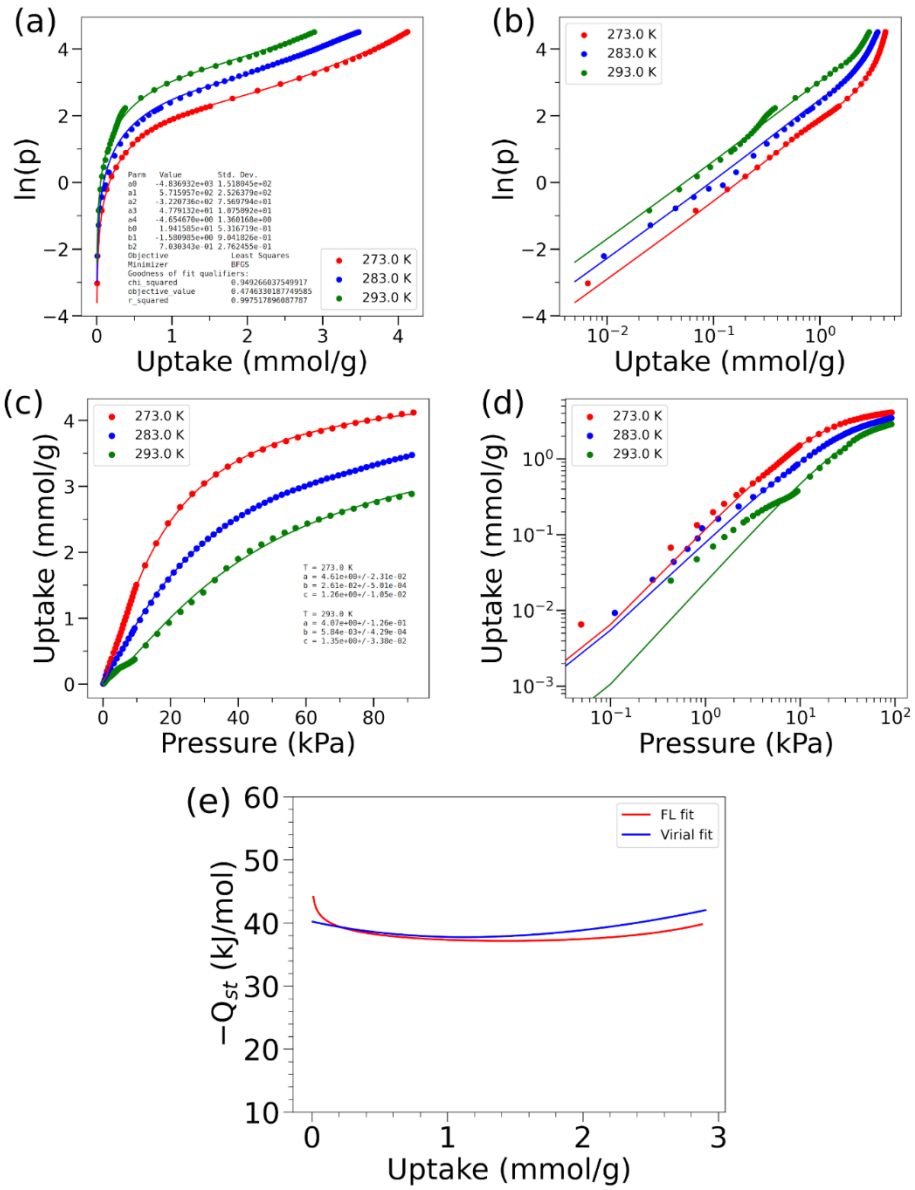

Fig. S9. (a)-(d) Measured adsorption isotherm data (filled circles) and the corresponding (a) & (b) virial and (c) & (d) Freundlich-Langmuir (FL) fits (solid lines) for C_2H_2 in Al-MOFM$_{15}$. (a) and (c) are reproduced with logarithmic scales in (b) and (d), respectively. (e) Isosteric heats of adsorption (Q_{st}) calculated using virial (blue) and FL fits (red), respectively. Q_{st} from virial fitting were estimated from the fits obtained for 273, 283, and 293 K isotherm data while that from FL-fits were estimated using the 273 and 293 K isotherm fits.

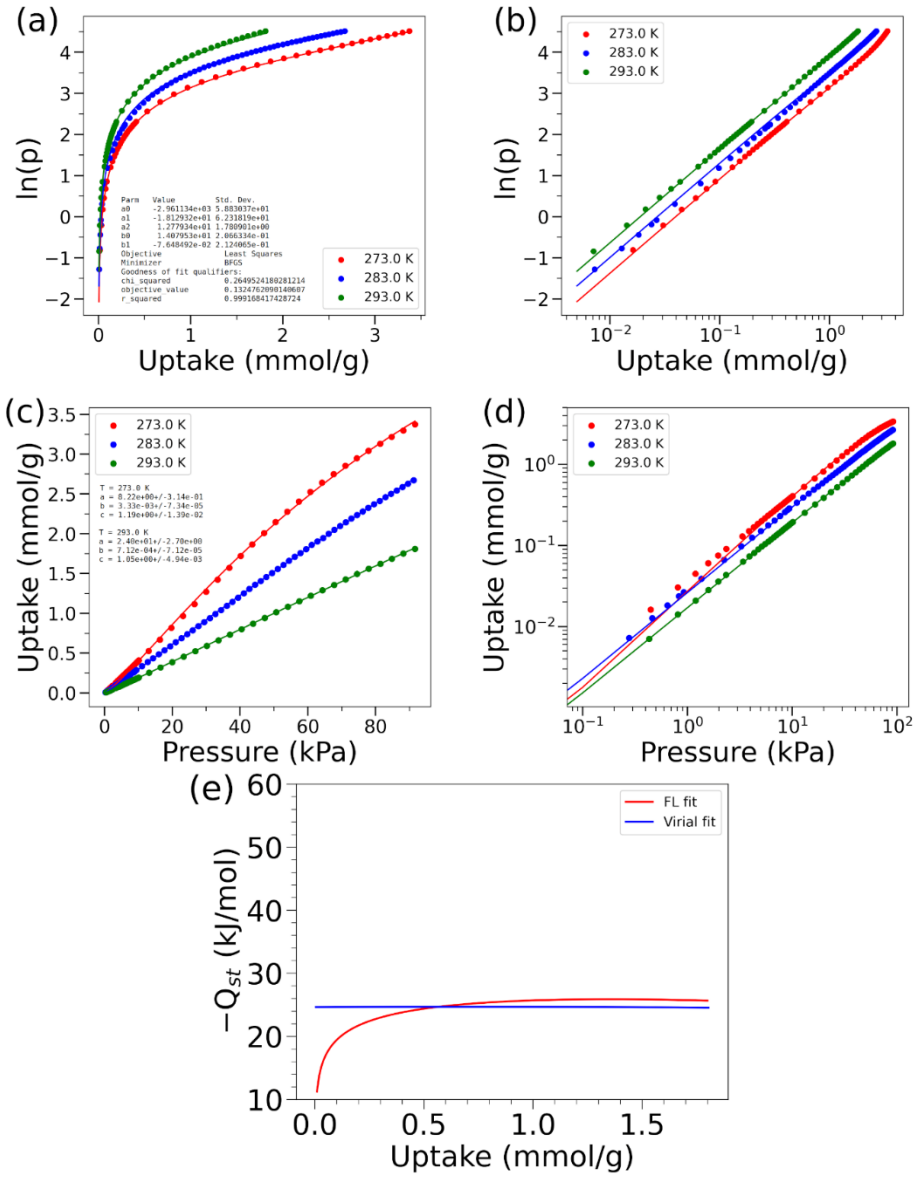

Fig. S10. (a)-(d) Measured adsorption isotherm data (filled circles) and the corresponding (a) & (b) virial and (c) & (d) Freundlich-Langmuir (FL) fits (solid lines) for CO_2 in Al-MOFM$_{15}$. (a) and (c) are reproduced with logarithmic scales in (b) and (d), respectively. (e) Isosteric heats of adsorption (Q_{st}) calculated using virial (blue) and FL fits (red), respectively. Q_{st} from virial fitting were estimated from the fits obtained for 273, 283, and 293 K isotherm data while that from FL-fits were estimated using the 273 and 293 K isotherm fits.

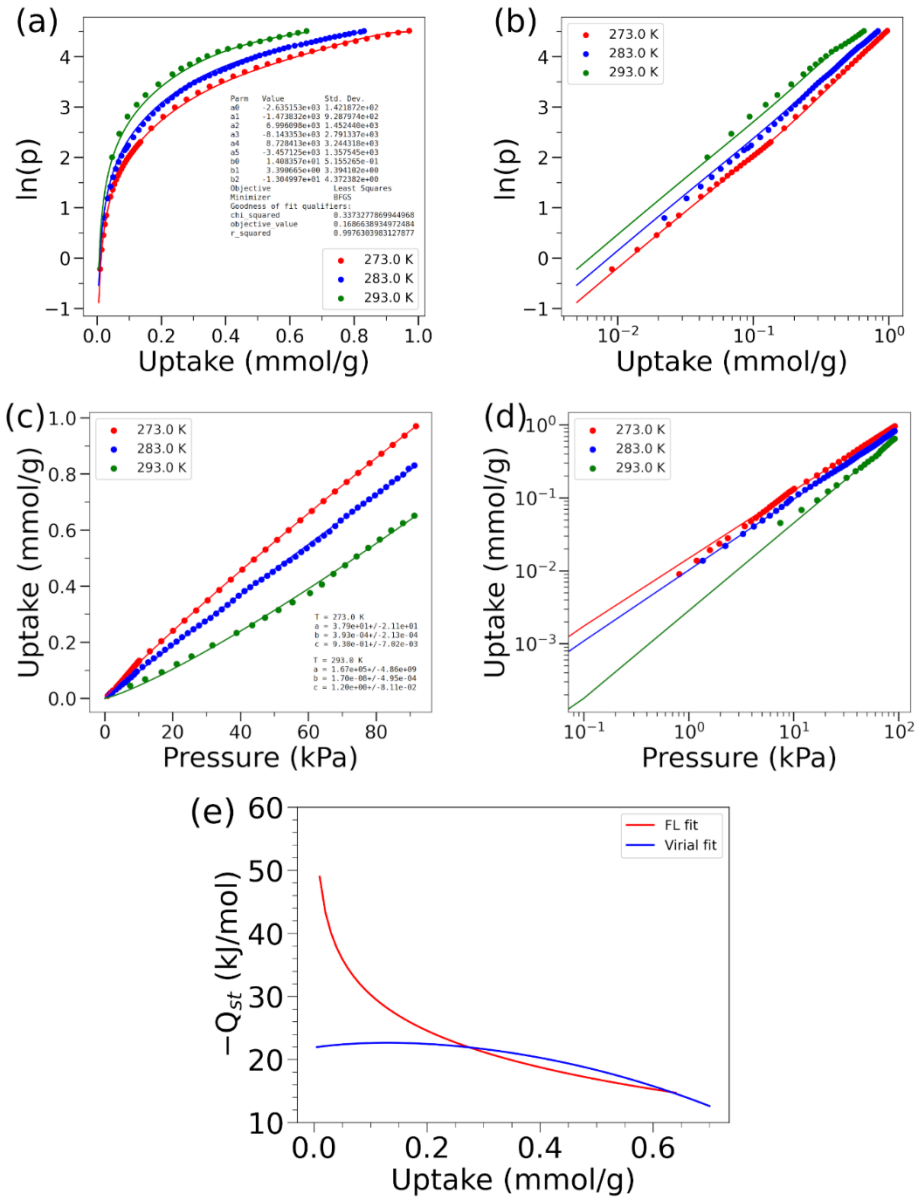

Fig. S11. (a)-(d) Measured adsorption isotherm data (filled circles) and the corresponding (a) & (b) virial and (c) & (d) Freundlich-Langmuir (FL) fits (solid lines) for CH_4 in Al-MOFM$_{15}$. (a) and (c) are reproduced with logarithmic scales in (b) and (d), respectively. (e) Isosteric heats of adsorption (Q_{st}) calculated using virial (blue) and FL fits (red), respectively. Q_{st} from virial fitting were estimated from the fits obtained for 273, 283, and 293 K isotherm data while that from FL-fits were estimated using the 273 and 293 K isotherm fits.

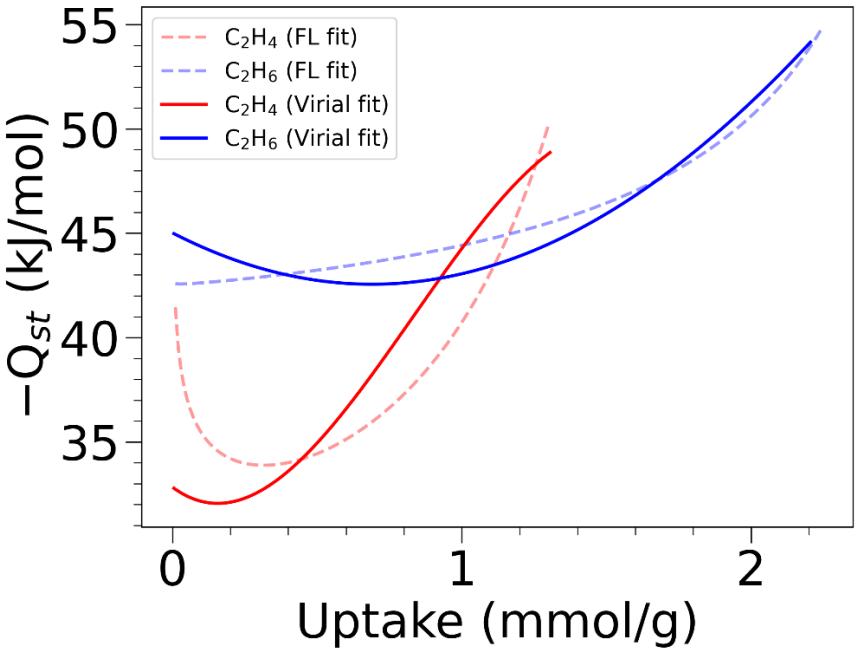

Fig. S12. Estimated coverage dependent isosteric heats of adsorption for C_2H_4 or C_2H_6 loading using virial and Freundlich-Langmuir (FL) fitting as indicated by the legend. A clear cross-over in the isosteric heats of adsorption w.r.t loading exists irrespective of the method employed to estimate them (virial at ~0.9 mmol/g and FL at ~1.1 mmol/g, respectively).

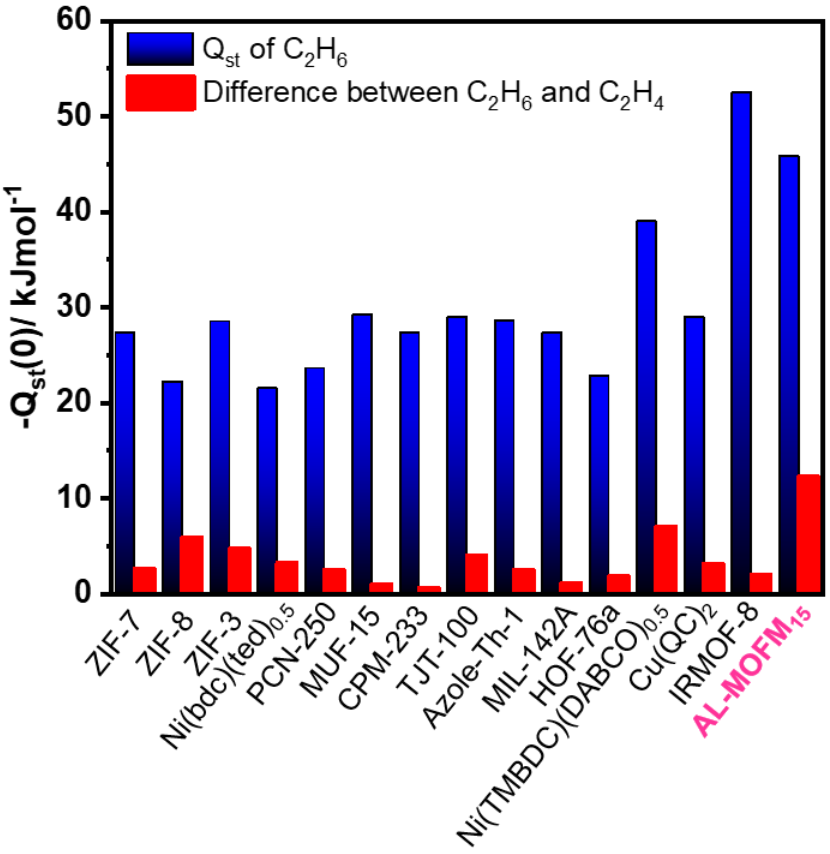

Fig. S13. Comparison of the isosteric heat of adsorption at zero loading ($Q_{st}(0)$) of C_2H_6 and C_2H_4 among representative porous materials.

Adsorption rate measurements

For diffusion, the relation of particle-vapor speed can be expressed by film thickness and diffusion coefficient. The graph represents $(C - C_{e1}/C_{01} - C_{e1})$ vs time (sec), where C is the density of the adsorbate. Additionally, C_{e1}, C_{01} are the gas phase density at equilibrium point and saturated vapor pressure by considering n-th (here we choose the 1st point where n=1) point at p/p_0. For measuring the adsorption rate from CO_2 and CH_4 adsorption, we choose the very first point or the zero coverage and the corresponding kinetic plot with LDF (linear driving force) fitting are as given below.[5, 6] Note that, at first point, the rate of adsorptions (k) are **0.184** and **2.25×10^{-3}** for CO_2 and CH_4, respectively.

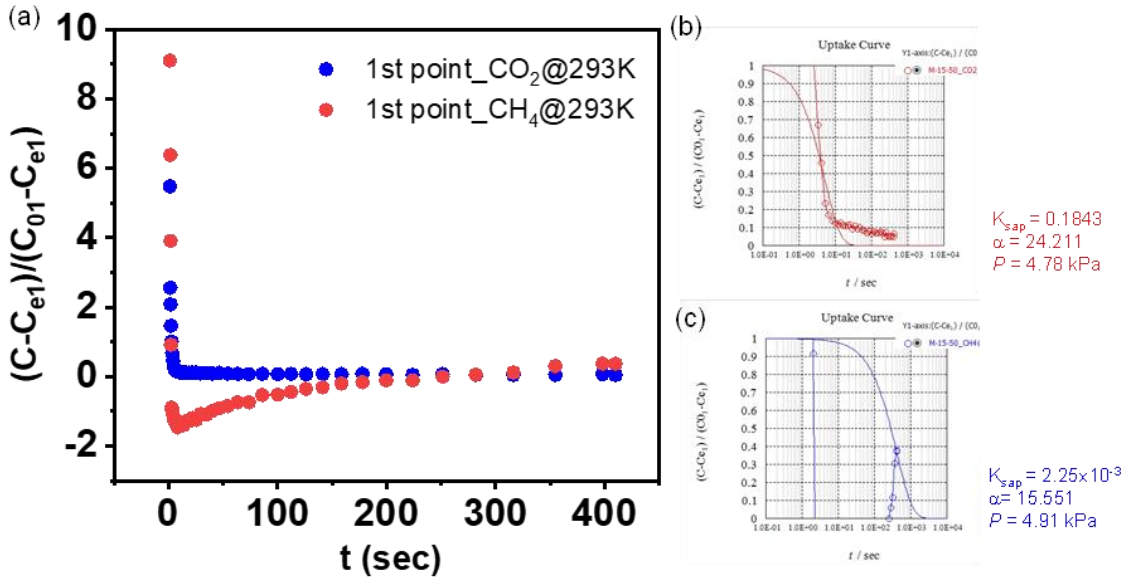

Fig. S14. (a) Adsorption rate measurement graph for CO_2 and CH_4 in Al-MOFM$_{15}$ at 293 K with respective (b, c) LDF fitting considering zero coverage adsorption point at ~ 4 kPa.

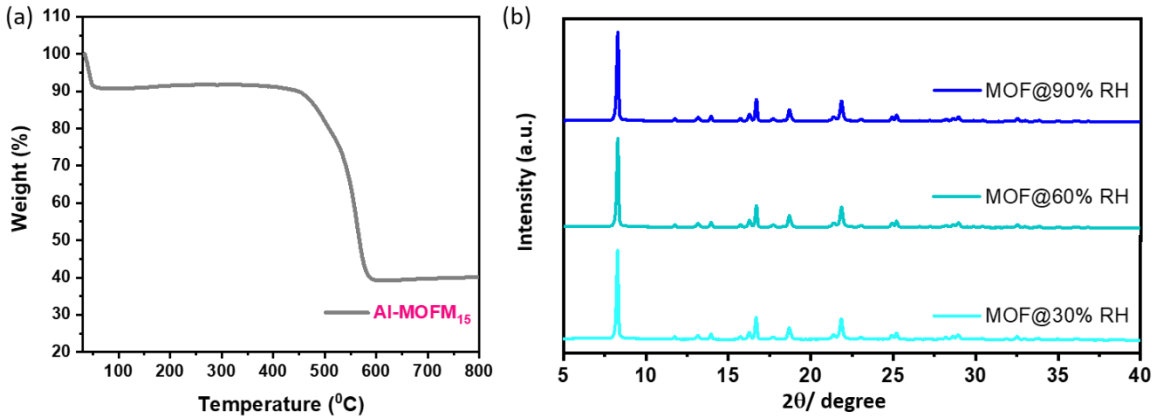

Fig. S15. (a) TGA thermogram represents the stability of the material under varied temperature and (b) PXRD of Al-MOFM$_{15}$, after treating the material under different humid conditions.

Computational details; on obtaining binding sites and the corresponding binding energies

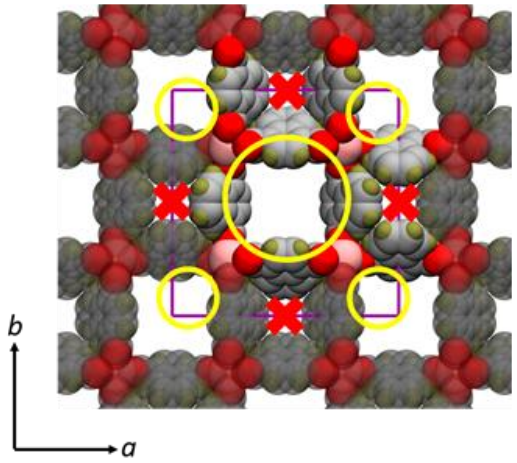

Fig. S16. Pore channels in a 1×1×2 supercell (purple square) of Al-MOF. Note that the replicated unit cell lies in plane of paper. Two small pore channels are indicated by red 'cross' marks and are forbidden for gas adsorption. Two large channels are indicated by yellow circles—one at the centre while the four corners of the supercell together constitute another large pore channel.

The initial configurations of one/multiple guest molecules in large pore channels of Al-MOF were obtained using the 'Adsorption Locator' module of the Materials Studio 2020 suite.[7] The adsorption locator module employs simulated annealing[8] algorithm to locate binding sites. A total of five Monte Carlo cycles with 50,000 steps per cycle was used. Translation, rotation,

regrowth moves were allowed for the guest molecules in a 1×1×2 supercell of Al-MOF constructed from the published CIF file;[9] only the two large pore channels were made available for the guest molecule insertion by blocking small pore channels by placing argon and helium atoms in them. The interaction energy of the MOF-guest system was calculated using a classical force field assuming a rigid framework. Lennard-Jones parameters for atoms of the framework and the guests were taken from the Universal Force Field (UFF).[9] The partial charges on the atoms were calculated for the periodic framework and the guests separately using the charge equilibration method.[10] Note that Q_{eq} assigned zero charge to helium/argon atoms inserted to block small pore channels, thus, not affecting the framework charges due to their presence.

Several binding sites were obtained for CO_2, CH_4, C_2H_2, C_2H_4, or C_2H_6 in the Al-MOF supercell. A few distinct configurations were selected for a given guest and then used as the initial configurations for binding energy calculations. Configurations of four/six C_2H_4/C_2H_6 molecules were also obtained. The configurations were classified based on how the guest molecules were distributed into the two large pore channels (Fig. S14) present in the simulation box. For example, simulation cells with four guest molecules can be classified into three categories--all the four in one channel, three in one and the other in the other channel, and two in each channel, called 4/0, 3/1, and 2/2 configurations, respectively. The same can be referred to as 2/0, 1.5/0.5, 1/1 configurations, i.e., based on the number of guest molecules per pore channel per unit cell. Similarly, six guest molecule (i.e., 3 molecules per unit cell) configurations were classified into four categories--3/0, 2.5/0.5, 2/1, and 1.5/1.5.

Mixture adsorption and selectivity study

The binary mixture adsorption isotherms and selectivity values were obtained using ideal adsorbed solution theory (IAST).[11] For IAST calculations, single component adsorption isotherms were fitted using Freundlich-Langmuir adsorption isotherm model:

$A = \frac{a\, bp^c}{1+bp^c}$, where A is adsorption uptake, p is pressure, and $a, b, and\ c$ are parameters for Freundlich-Langmuir isotherm model.

Table S2: Fitted Freundlich-Langmuir isotherm model parameters for different gases.

	Temperature (K)	a (mol/kg)	b(Pa^{-c})	c
CO_2	273	184.02	9.15e-7	1.19
CH_4	273	476.97	1.04e-6	0.94
C_2H_2	273	103.37	4.2e-6	1.26
C_2H_4	273	73.35	1.33e-5	1.09
C_2H_6	273	72.38	9.44e-6	1.26
CO_2	293	537.83	5.01e-7	1.05
CH_4	293	298.00	4.25e-8	1.22
C_2H_2	293	96.24	4.4e-6	1.14
C_2H_4	293	38.82	3.22e-6	1.21
C_2H_6	293	62.07	2.17e-6	1.26

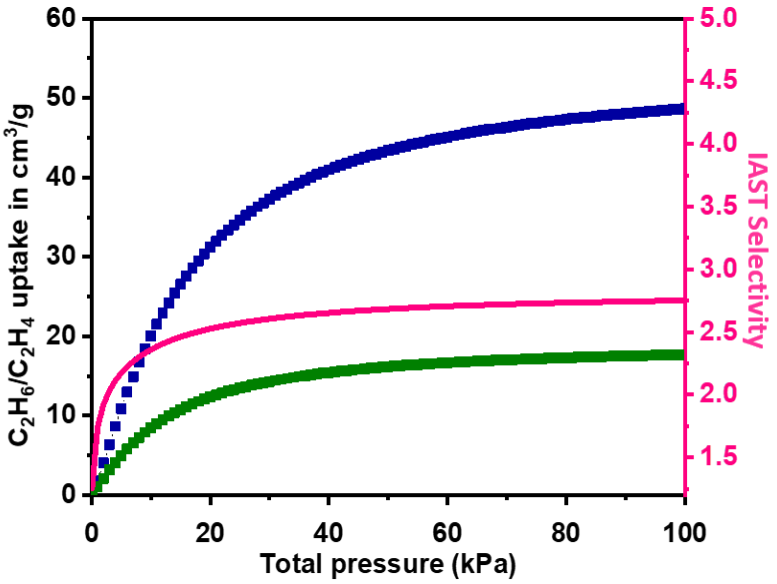

Fig. S17. Predicted mixture adsorption isotherm and IAST selectivity of Al-MOFM$_{15}$ for C_2H_6/C_2H_4 (50:50) at 273 K. Uptake for C_2H_6 and C_2H_4 are represented in dark blue and green, respectively.

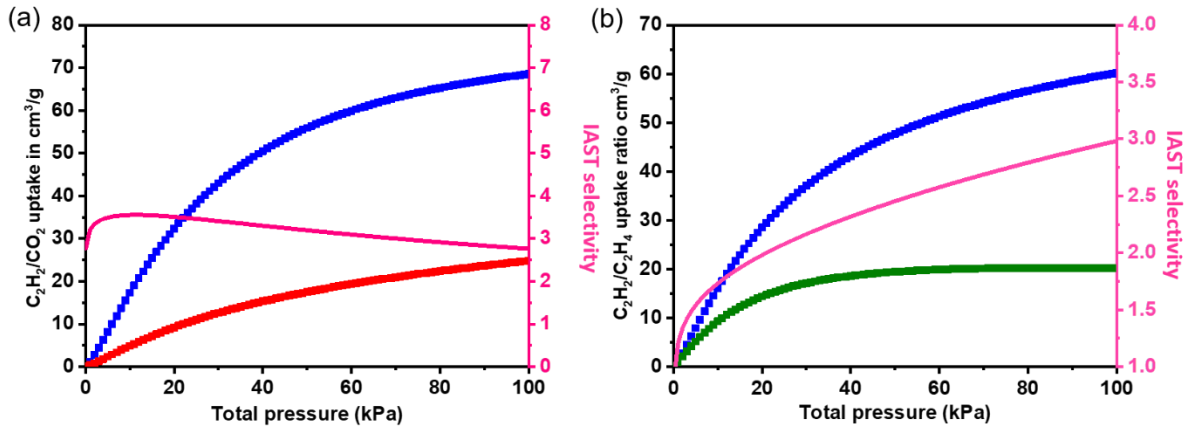

Fig. S18. Predicted mixture adsorption isotherm and IAST selectivity of Al-MOFM$_{15}$ for (a) C_2H_2/CO_2 (50:50), (b) C_2H_2/C_2H_4 (50:50) at 273 K. Uptake for C_2H_2, CO_2 and C_2H_4 are represented in blue, red and green, respectively.

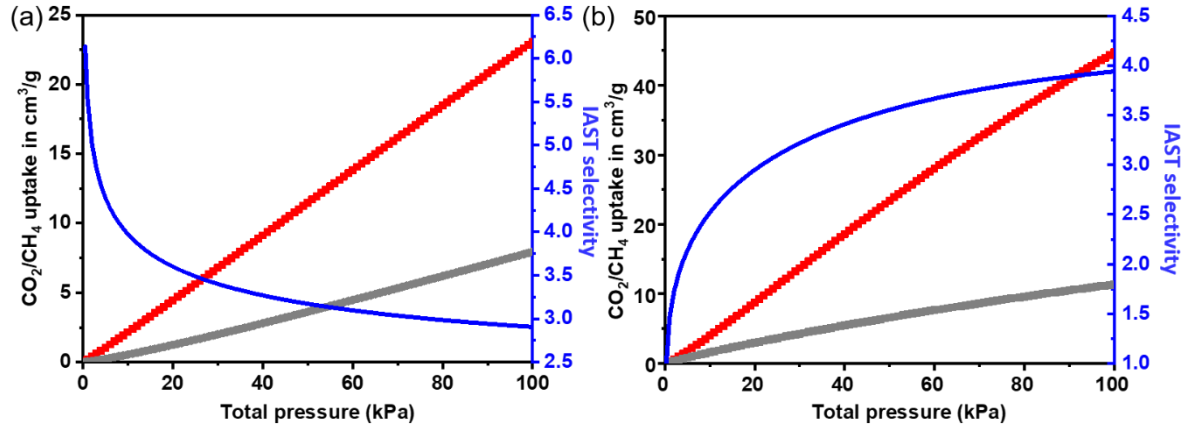

Fig. S19. Predicted mixture adsorption isotherm and IAST selectivity of Al-MOFM$_{15}$ for (a) CO_2/CH_4 (50:50), (b) CO_2/CH_4 (50:50) at 293 and 273 K, respectively. Uptake for CO_2 and CH_4 are represented in red and grey, respectively.

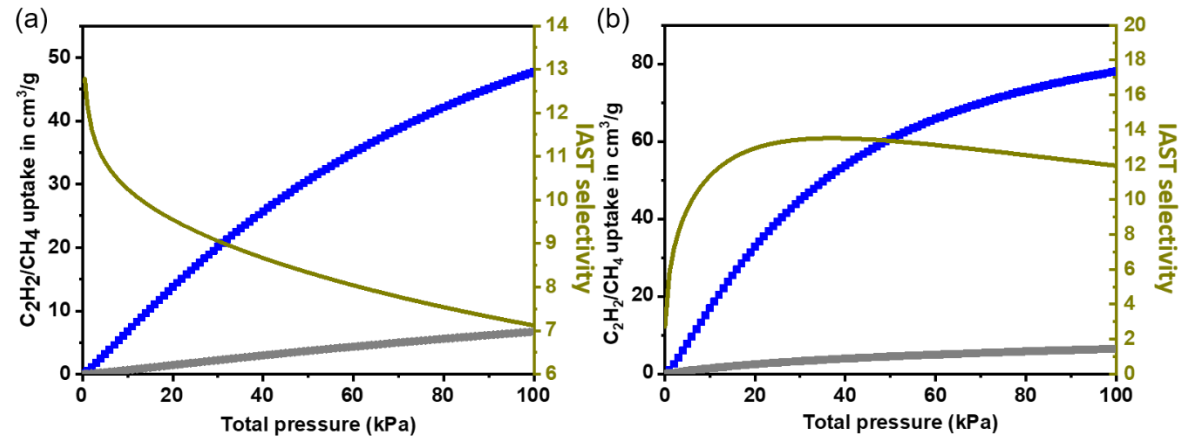

Fig. S20. Predicted mixture adsorption isotherm and IAST selectivity of Al-MOFM$_{15}$ for (a) C_2H_2/CH_4 (50:50), (b) C_2H_2/CH_4 (50:50) at 293 and 273 K, respectively. Uptake for C_2H_2 and CH_4 are represented in blue and grey, respectively.

Table S3: Calculated IAST selectivity and mixed gas uptake ratio at 100 kPa for specific hydrocarbon combinations.

Gas mixture A:B (50:50)	**IAST selectivity**		**Mixed gas uptake (A) in cm^3/g**		**Mixed gas uptake (B) in cm^3/g**	
	273 K	**293 K**	**273 K**	**293 K**	**273 K**	**293 K**
C_2H_6/C_2H_4	2.75	2.51	48.64	29.85	17.67	11.94
C_2H_2/CO_2	2.76	2.54	68.51	44.65	24.8	17.54
C_2H_2/C_2H_4	2.98	3.32	60.21	37.91	20.19	11.38
CO_2/CH_4	3.93	2.90	44.73	23.06	11.53	7.94
C_2H_2/CH_4	11.94	7.11	78.06	47.76	6.53	6.70

DFT calculations

Density functional theory (DFT) calculations in this work were carried out using the CP2K package version-7.1[12, 13] using Gaussian Plane Wave (GPW) method implemented in the QUICKSTEP[14] module. Perdew-Burke-Ernzerhof (PBE)[15] exchange-correlation (XC) functional with Grimme-D3[16, 17] dispersion correction method was employed. Goedecker-Teter-Hutter (GTH) psuedo-potentials[18-20] was used to represent the core electrons. Triple-ζ with two sets of polarization functions basis sets optimized for molecular calculations (TZV2P-MOLOPT-GTH)[21] were used to represent the valence electrons of hydrogen, carbon, and oxygen while the short range variant (TZV2P-MOLOPT-SR-GTH) was used for aluminium. Five multi-grids for mapping electron density were used. Plane wave and relative cut-offs were set to 600 and 60 Ry, respectively. The inner and outer SCF convergence criteria were set to 1.0×10^{-7} Ha. Poisson solver (with XYZ periodicity) was employed to calculate the electrostatic potential contribution to the Hamiltonian. A simulation box comprising of 1×1×2 Al-MOF unit

cells was used for all DFT calculations. A 3.4% relative change in volume of the simulation box after cell optimization exhibit the robustness of the DFT parameters employed.

Geometry Optimization: The built-in 'GEO_OPT' feature in CP2K employing BFGS optimizer was used for geometry optimizations of pristine or guest loaded Al-MOF simulation cells. All the atoms in the simulation box were relaxed during optimization. Root mean square and maximum force convergence were set to 3.0×10^{-4} and 4.5×10^{-4} Ha·Å^{-1}, respectively. The initial configurations of the simulation cells loaded with one or more guest molecules were obtained using Materials studio as described in the previous section.

Binding energy and adsorbate-adsorbate interaction energy calculations: Binding energy (BE) quantifies the strength of guest-framework interactions. Three SCF cycle calculations, to obtain total energy of a geometry optimized simulation cell comprising of (1) the whole system, i.e., framework and guest(s) ($E_{fw+guest}$), (2) framework (E_{fw}), and (3) one guest molecule (E_{guest}) is required to determine the binding energy of guest molecule(s) using the following expression,

$$BE = \frac{E_{fw+guest} - (E_{fw} + n \times E_{guest})}{n},$$

where 'n' is the number of guest molecules.

The extent to which the guest molecules cooperate (for n>1) amongst themselves is quantified by adsorbate-adsorbate interaction energy or cooperativity (E_c).

$$Ec = \frac{n \times E_{guest} - E_{guest*}}{n},$$

where E_{guest*} is the total energy of the guest molecules in the simulation box without the presence of any other atom.

Table S4: Comparison of range of DFT calculated binding energies (BE) against isosteric heat of adsorption estimated by virial fitting (Q_{st}) of the experimental isotherms at near-zero coverage for various guest molecules in Al-MOF.

Guest	**# of independent calculations**	**BE**	**Q_{st}(0) (virial)**
		kJ/mol	

CO_2	5	-19.1 to -36.0	-24.6
C_2H_2	4	-34.5 to -37.3	-40.2
C_2H_4	5	-33.2 to -38.7	-32.8
C_2H_6	6	-34.8 to -39.9	-45.0
CH_4	3	-25.2 to -25.4	-22.0

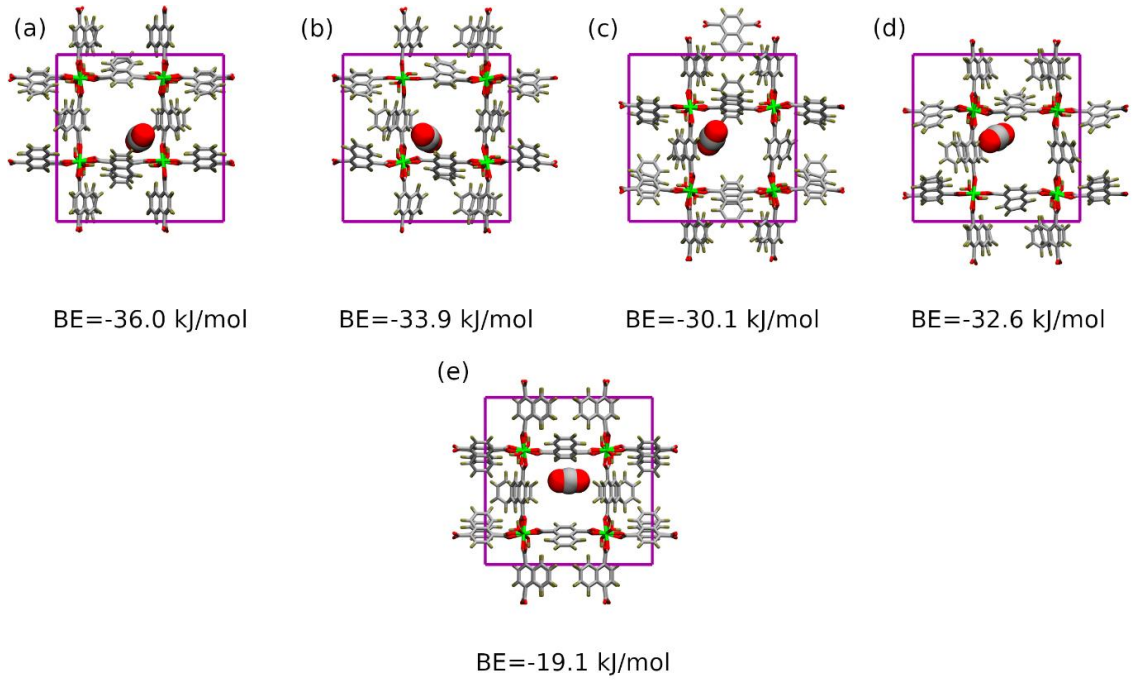

Fig. S21: Binding sites and the corresponding binding energies (BE) for a CO_2 molecule in a large pore of Al-MOF obtained by DFT optimizations.

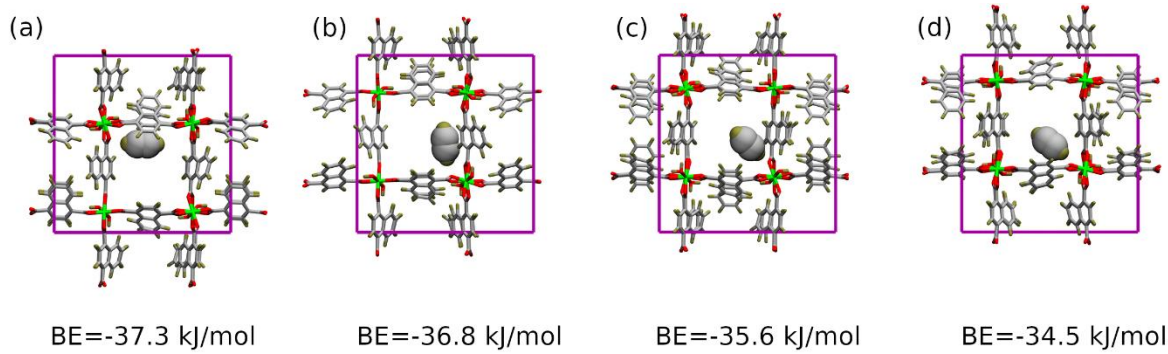

Fig. S22. Binding sites and the corresponding binding energies (BE) for a C_2H_2 molecule in a large pore of Al-MOF obtained by DFT optimizations.

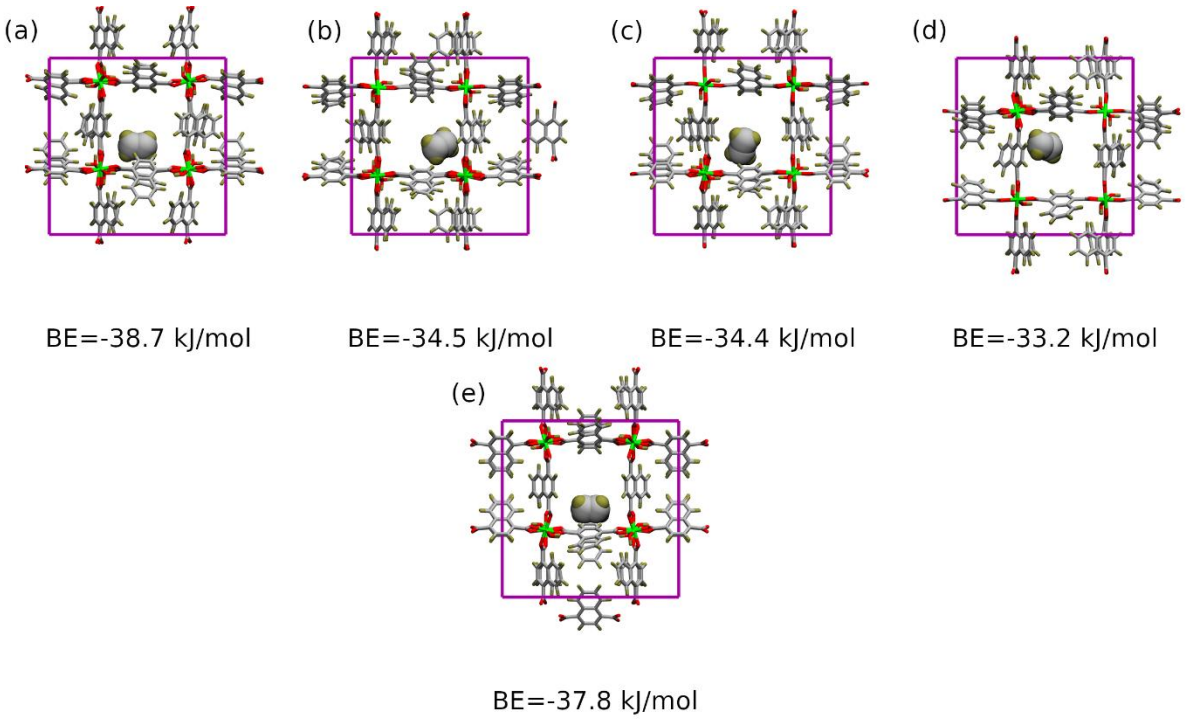

Fig. S23. Binding sites and the corresponding binding energies (BE) for a C_2H_4 molecule in a large pore of Al-MOF obtained by DFT optimizations.

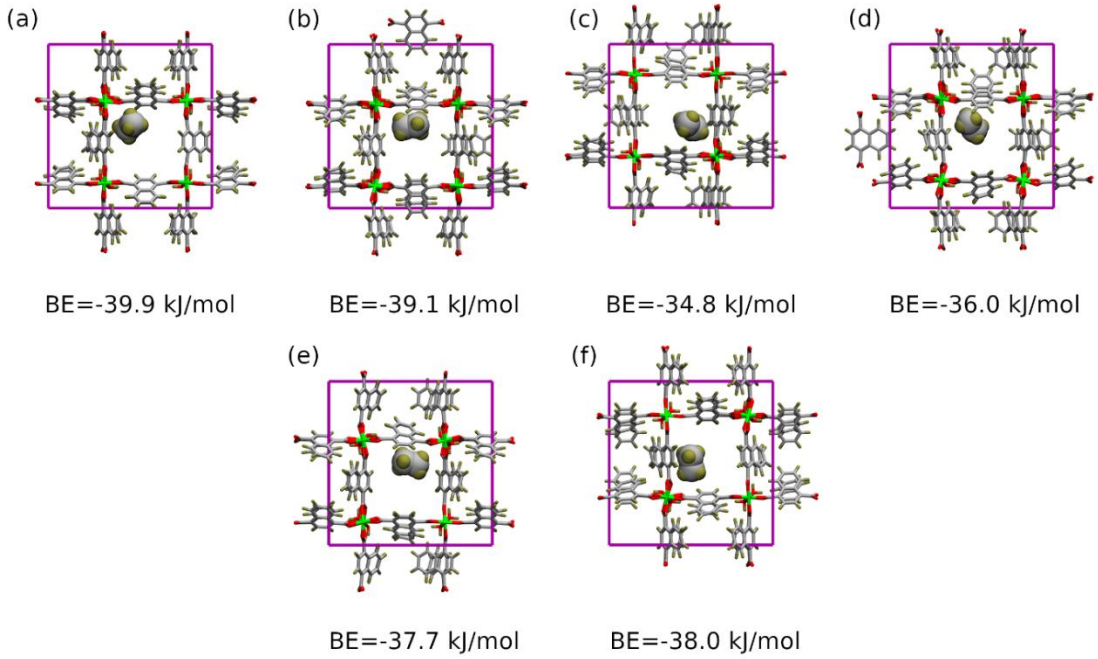

Fig. S24. Binding sites and the corresponding binding energies (BE) for a C_2H_6 molecule in a large pore of Al-MOF obtained by DFT optimizations.

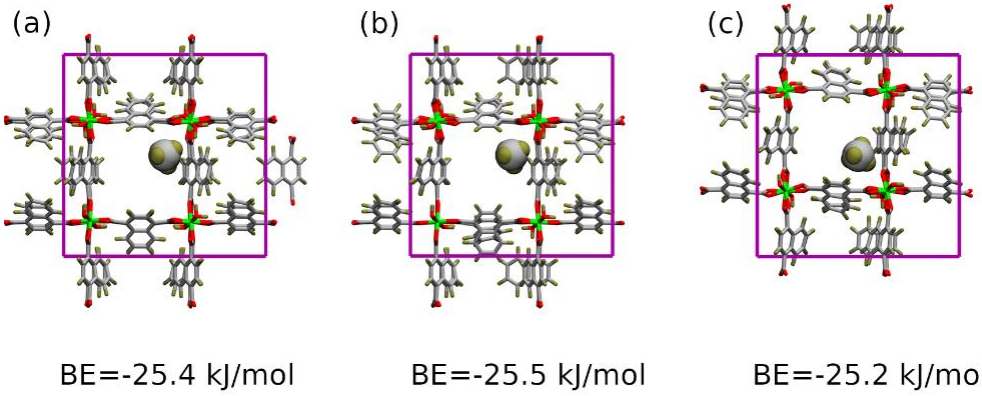

Fig. S25. Binding sites and the corresponding binding energies (BE) for a CH_4 molecule in a large pore of Al-MOF obtained by DFT optimizations.

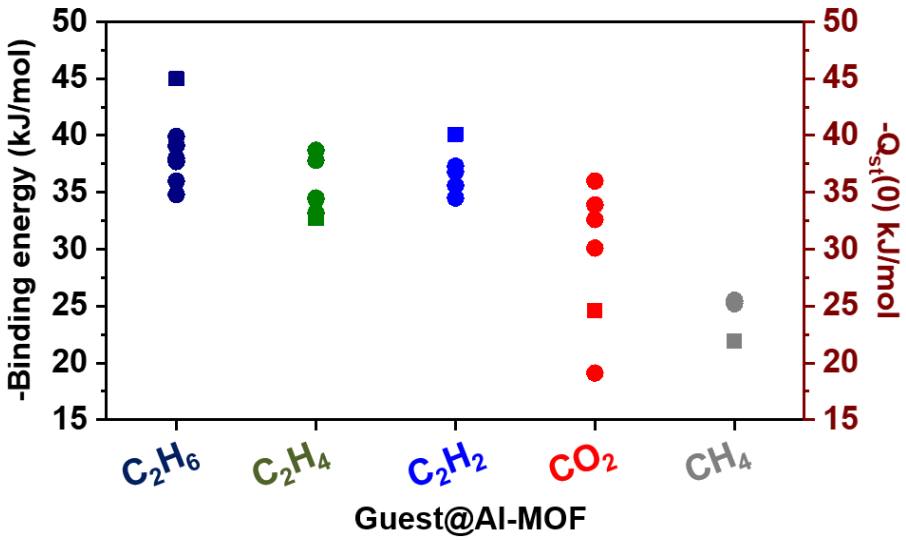

Fig. S26. Range of calculated binding energies and $Q_{st}(0)$ for the five guest molecules. Closed circles and squares are representing the BE and $Q_{st}(0)$, respectively.

Table S5: Binding energy (BE) and cooperativity (E_c) for Al-MOF loaded with two or three molecules per unit cell with C_2H_4/C_2H_6 in various configurations.

Guest	mol/UC	configuration	#independent calculations	BE	E_c
				kJ/mol	
C_2H_4	2	2/0	1	-41.1	-3.0
		1.5/0.5	5	-34.6 to -40.6	-1.4 to -3.6
		1/1	5	-35.1 to -37.3	-0.4 to -2.6
	3	3/0	3	-40.2 to -41.1	-5.6 to -6.9
		2.5/0.5	3	-39.2 to -41.1	-3.9 to -4.8
		2/1	6	-38.0 to -40.9	-2.8 to -3.7
		1.5/1.5	6	-36.4 to -40.6	-2.6 to -4.0
C_2H_6	2	2/0	1	-43.1	-3.8
		1.5/0.5	6	-35.8 to -40.3	-1.9 to -3.9
		1/1	4	-38.0 to -42.0	-1.9 to -3.6
	3	3/0	0	--	--
		2.5/0.5	3	-39.0 to -41.6	-5.1 to -6.6
		2/1	7	-37.5 to -41.8	-2.8 to -4.4
		1.5/1.5	8	-37.1 to -41.3	-3.0 to -4.7

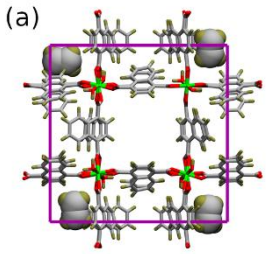

BE=-41.1 kJ/mol
Ec=-3.0 kJ/mol

Fig. S27. Locations of the four C_2H_4 molecules in a channel in its 2/0 configuration obtained from DFT optimization.

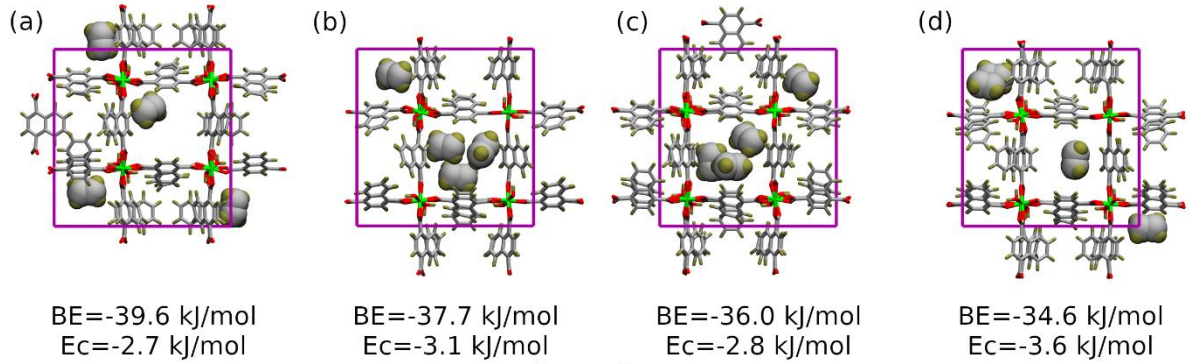

BE=-39.6 kJ/mol
Ec=-2.7 kJ/mol

BE=-37.7 kJ/mol
Ec=-3.1 kJ/mol

BE=-36.0 kJ/mol
Ec=-2.8 kJ/mol

BE=-34.6 kJ/mol
Ec=-3.6 kJ/mol

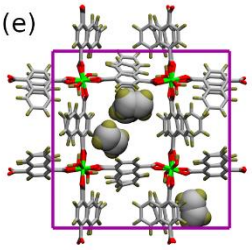

BE=-37.4 kJ/mol
Ec=-1.4 kJ/mol

Fig. S28. Various 1.5/0.5 configurations of C_2H_4 with three molecules in one pore channel and one in the other obtained by DFT optimizations.

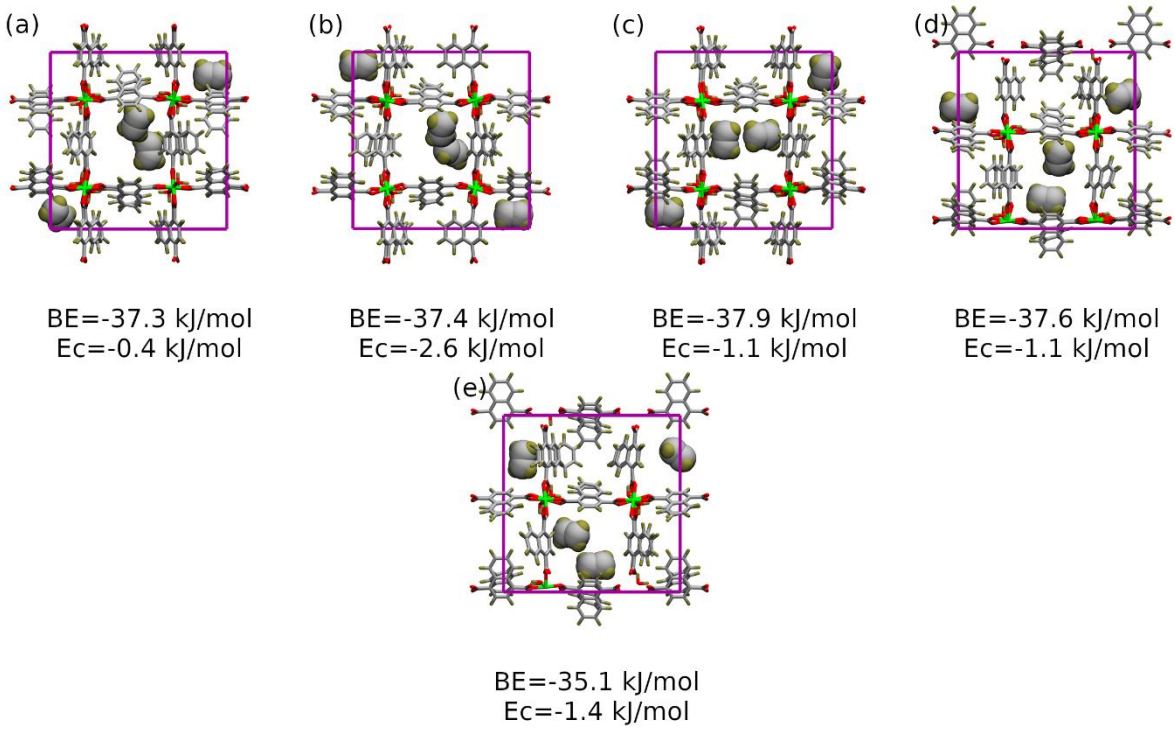

Fig. S29. Various 1/1 configurations of C_2H_4 with two molecules in one pore channel each obtained by DFT optimizations.

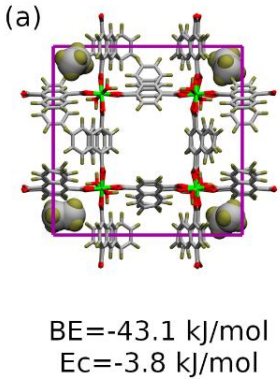

Fig. S30. Locations of the four C_2H_6 molecules in a channel in its 2/0 configuration obtained from DFT optimization.

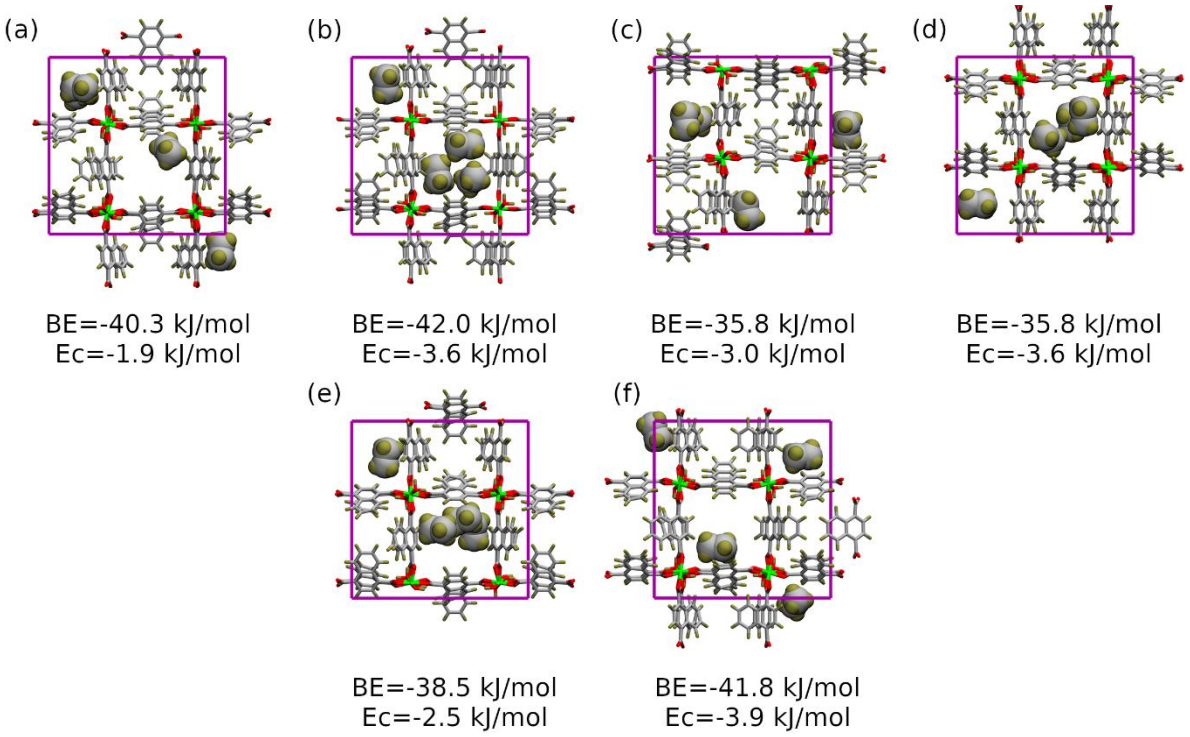

Fig. S31. Various 1.5/0.5 configurations of C_2H_6 with three molecules in one pore channel and one in the other obtained by DFT optimizations.

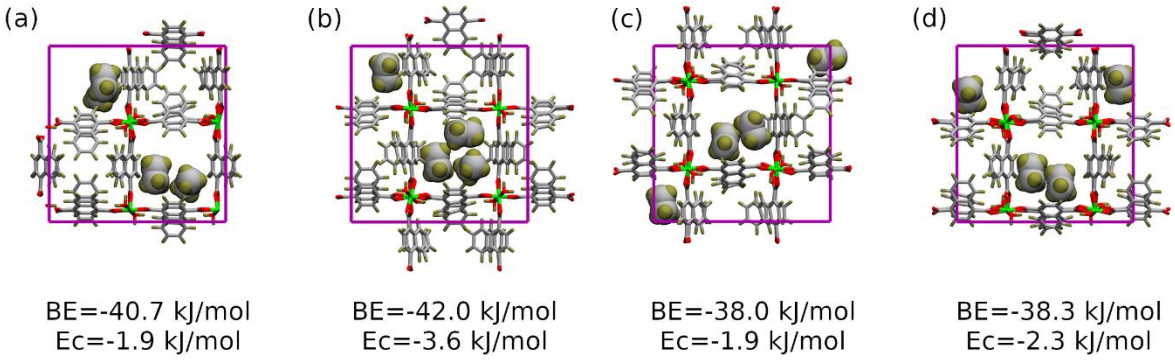

Fig. S32. Various 1/1 configurations of C_2H_6 with two molecules in one pore channel each obtained by DFT optimizations.

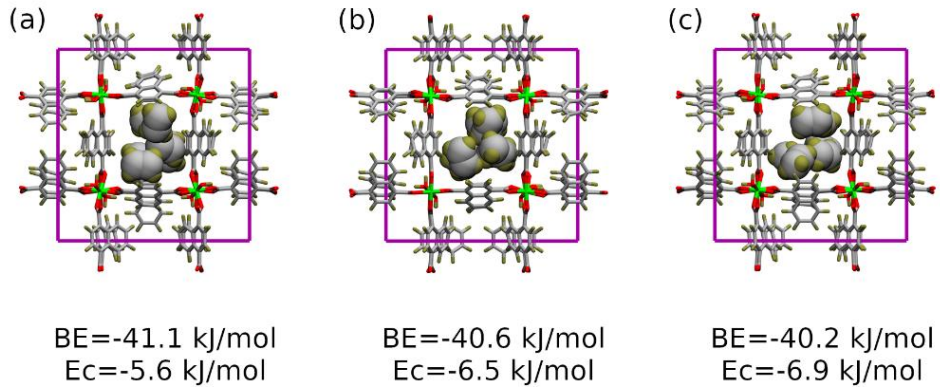

Fig. S33. Various 3/0 configurations of C_2H_4 with all six molecules in one pore channel obtained by DFT optimizations.

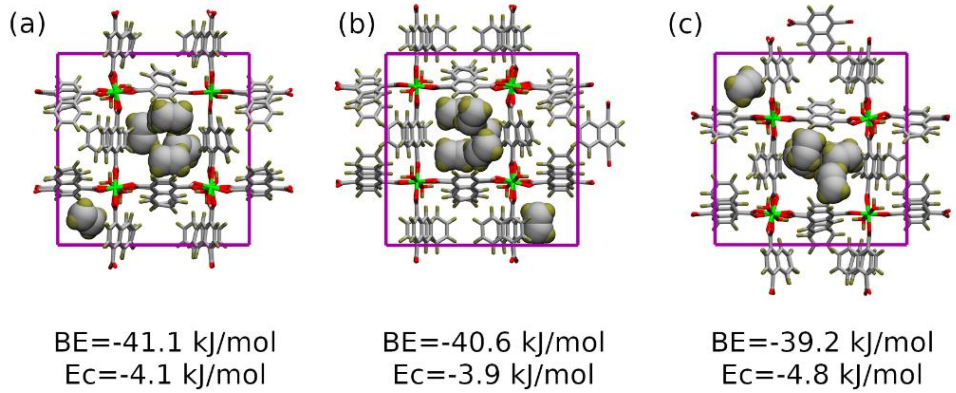

Fig. S34. Various 2.5/0.5 configurations of C_2H_4 with five molecules in one pore channel and the other in the other pore channel obtained by DFT optimizations.

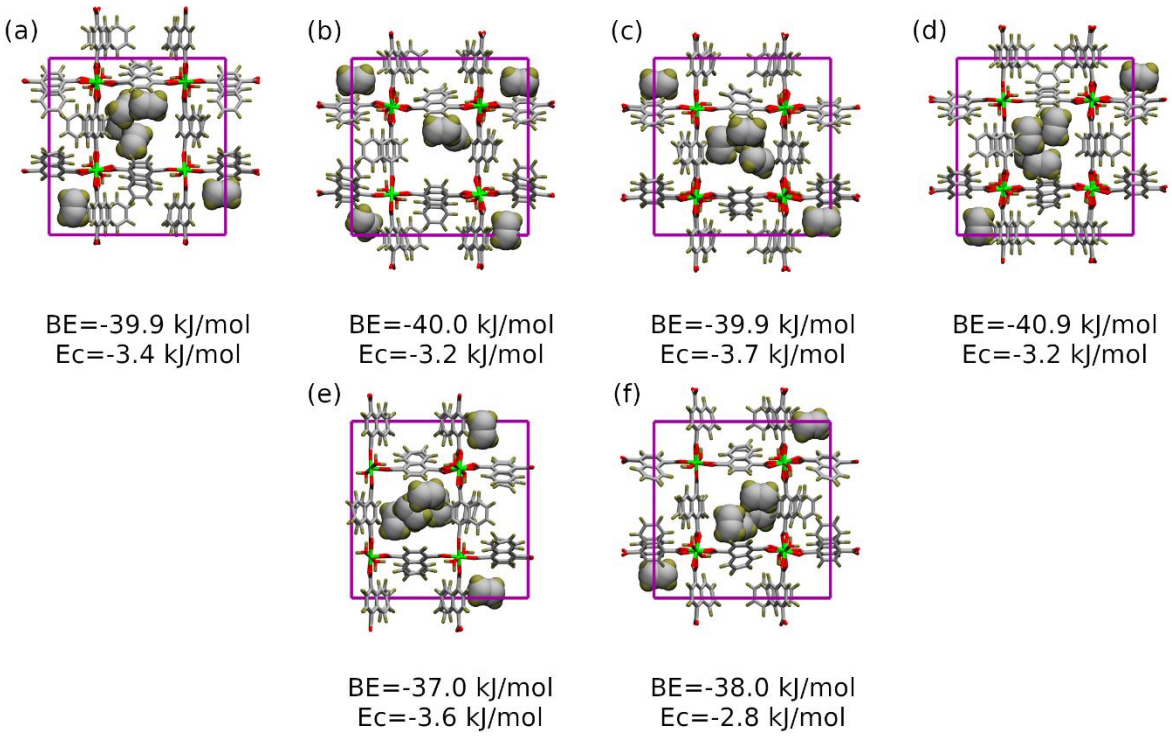

Fig. S35. Various 2/1 configurations of C_2H_4 with four molecules in one pore channel and two others in the other pore channel obtained by DFT optimizations.

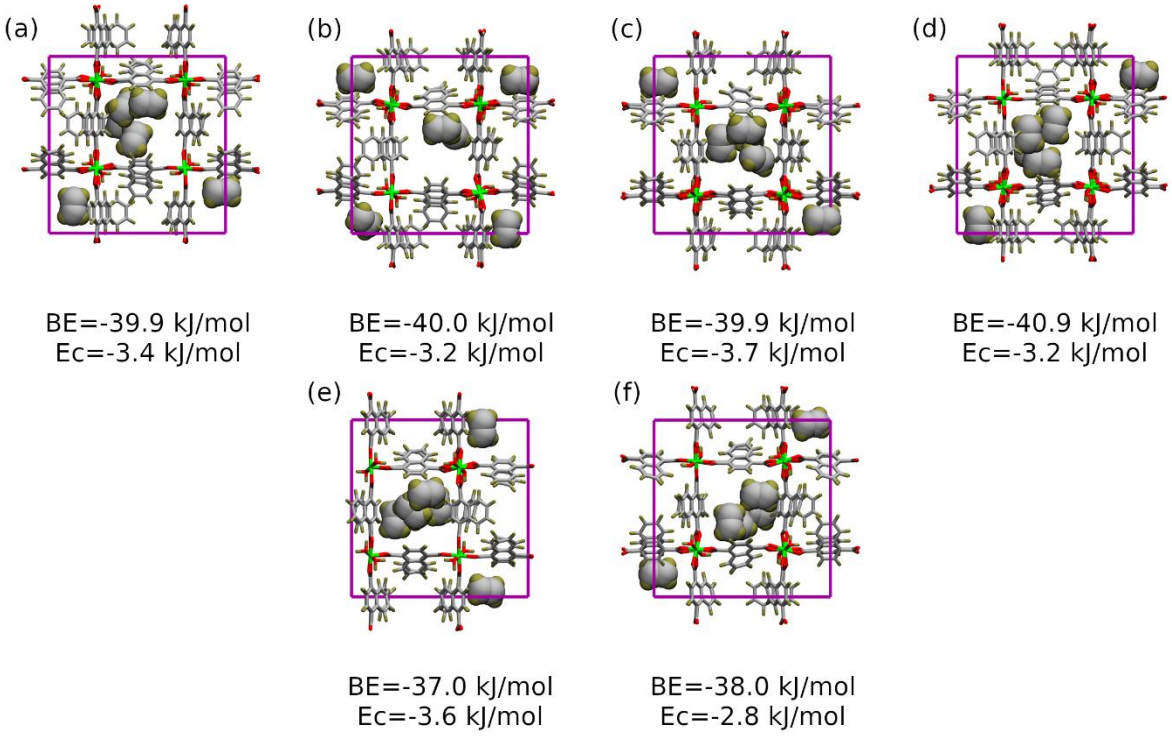

Fig. S36. Various 1.5/1.5 configurations of C_2H_4 with three molecules in each pore channel obtained by DFT optimizations.

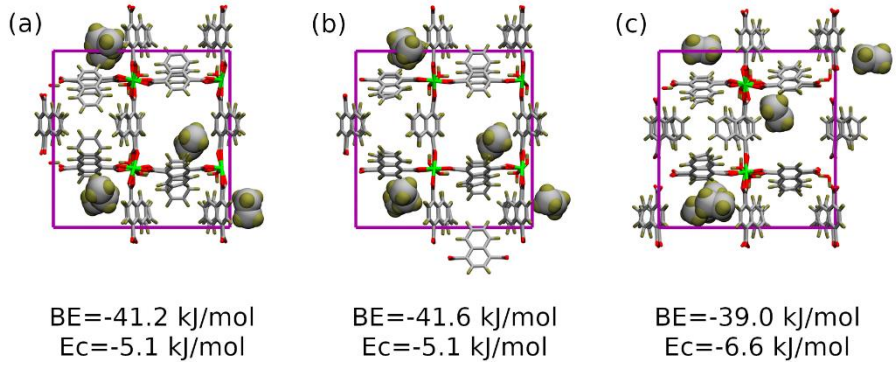

Fig. S37. Various 2.5/0.5 configurations of C_2H_6 with five molecules in one pore channel and the other in the other pore channel obtained by DFT optimizations.

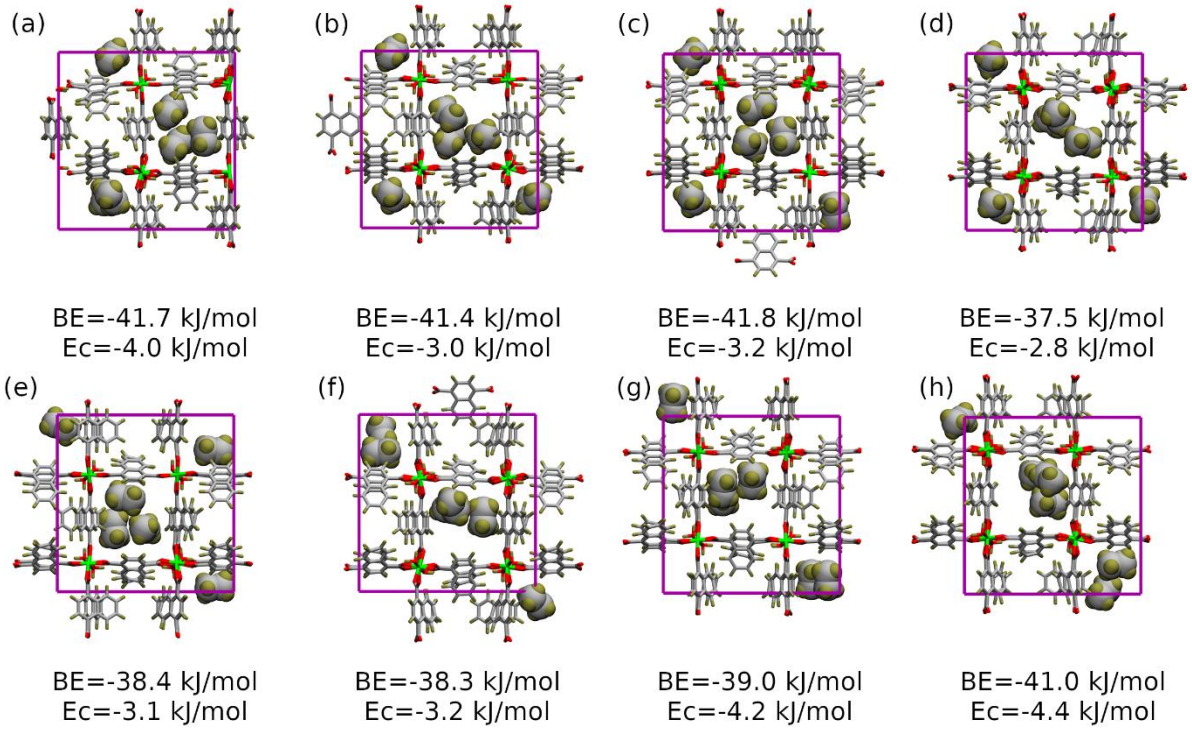

Fig. S38. Various 2/1 configurations of C_2H_6 with four molecules in one pore channel and two others in the other pore channel obtained by DFT optimizations.

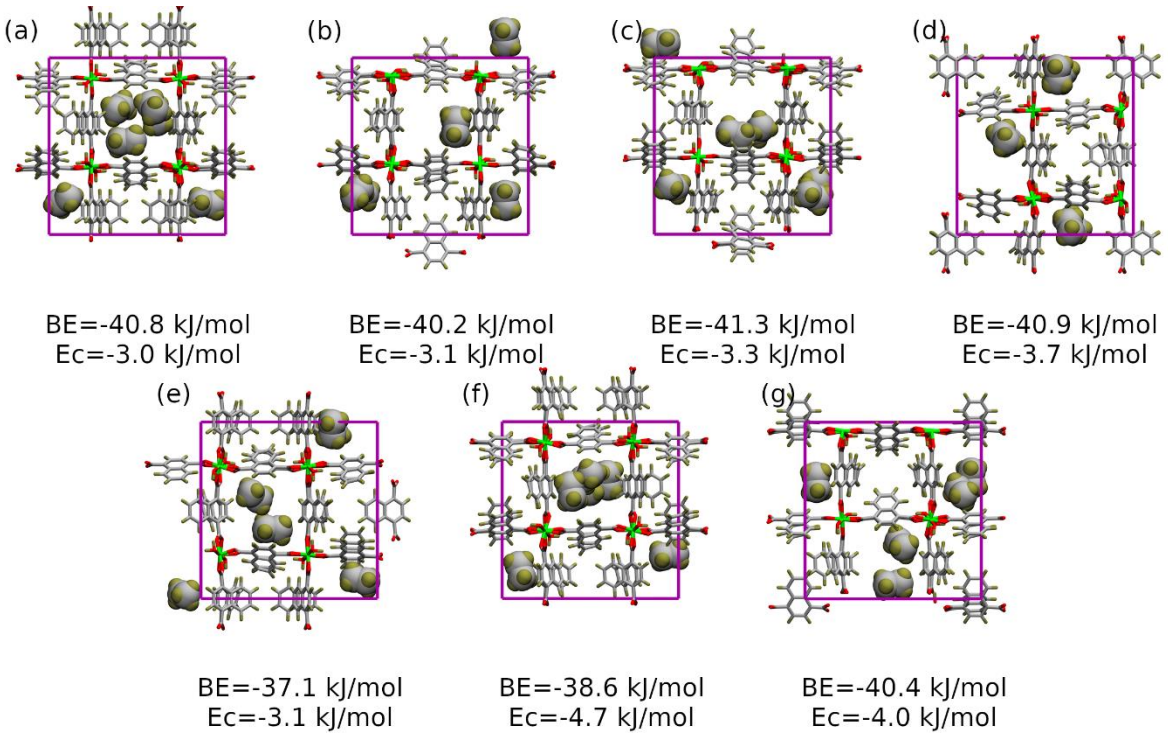

Fig. S39. Various 1.5/1.5 configurations of C_2H_6 with three molecules in each pore channel obtained by DFT optimizations.

Ab initio molecular dynamics (AIMD) simulations

Ab initio molecular dynamics (AIMD) simulations of Al-MOF simulation box without any guest molecules in NVT-ensemble at 293 K was carried out. The equations of motion were integrated with a time step of 0.5 fs with the forces calculated using DFT parameters mentioned in the previous section. The temperature was fixed using the CSVR[22] thermostat with a damping constant of 100 fs. The system was equilibrated for ~4.5 ps before generation of a 5 ps trajectory.

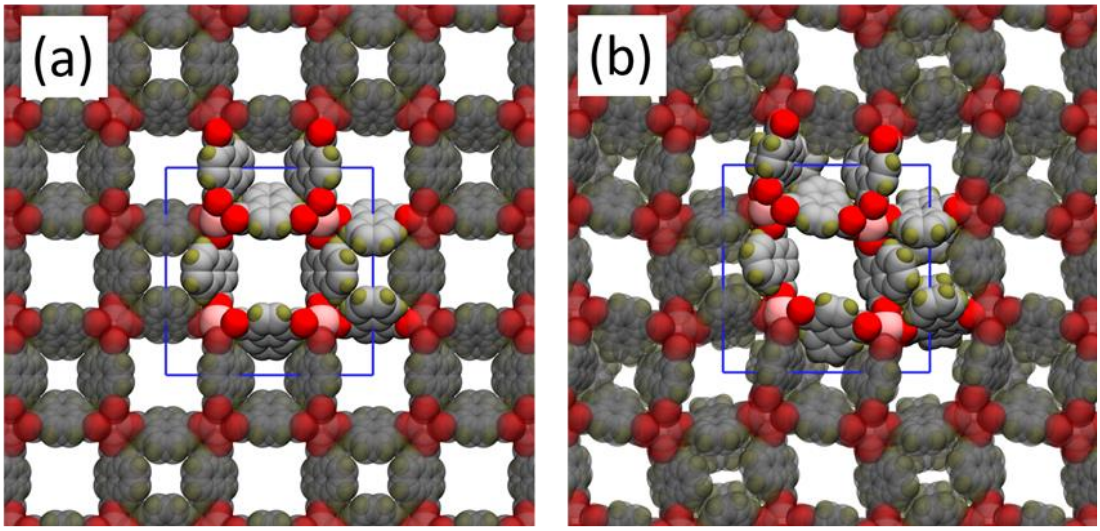

Fig. S40. Shows (a) The Al-MOF crystal structure and (b) a snapshot from the AIMD trajectory at 293 K. The periodic images (dark & transparent) are also shown along with the atoms in the simulations cell (bright & opaque). (b) clearly shows the closing of small pore channels. Supplementary movie of the AIMD trajectory also shows spontaneous closure of small pore channels at the start of the simulation and which continue to remain closed during the course of the simulation.

Grand canonical Monte Carlo (GCMC) simulations

Grand Canonical Monte Carlo (GCMC) simulations a 2×2×5 super cell of Al-MOF was performed using the RASPA-2.0[23-25] package. Given pressures was converted into fugacities, a GCMC control parameter using the Peng-Robinson equation of state. Translation, rotation, insertion, and deletion moves of guest molecules while no moves neither of the framework atoms nor on the internal degrees of freedom the guest molecules were exercised during the simulations. Lennard-Jones (LJ) parameters for the framework atoms were taken from the Universal Force Field (UFF)[26] while the point charges on the atoms were assigned using the DDEC6[27] charge partitioning scheme. Transferable potentials for phase equilibria (TraPPE)[28-32] was used for CO_2, CH_4, C_2H_4, and C_2H_6. The three hydrocarbons used the United Atom (UA) flavour of TraPPE with no partial charges on their constituting atoms.

Isotherms were calculated at 273 K and 293 K by (a) unrestricted occupation of molecules in small and large pore channels and (b) blocking the small pore channels.

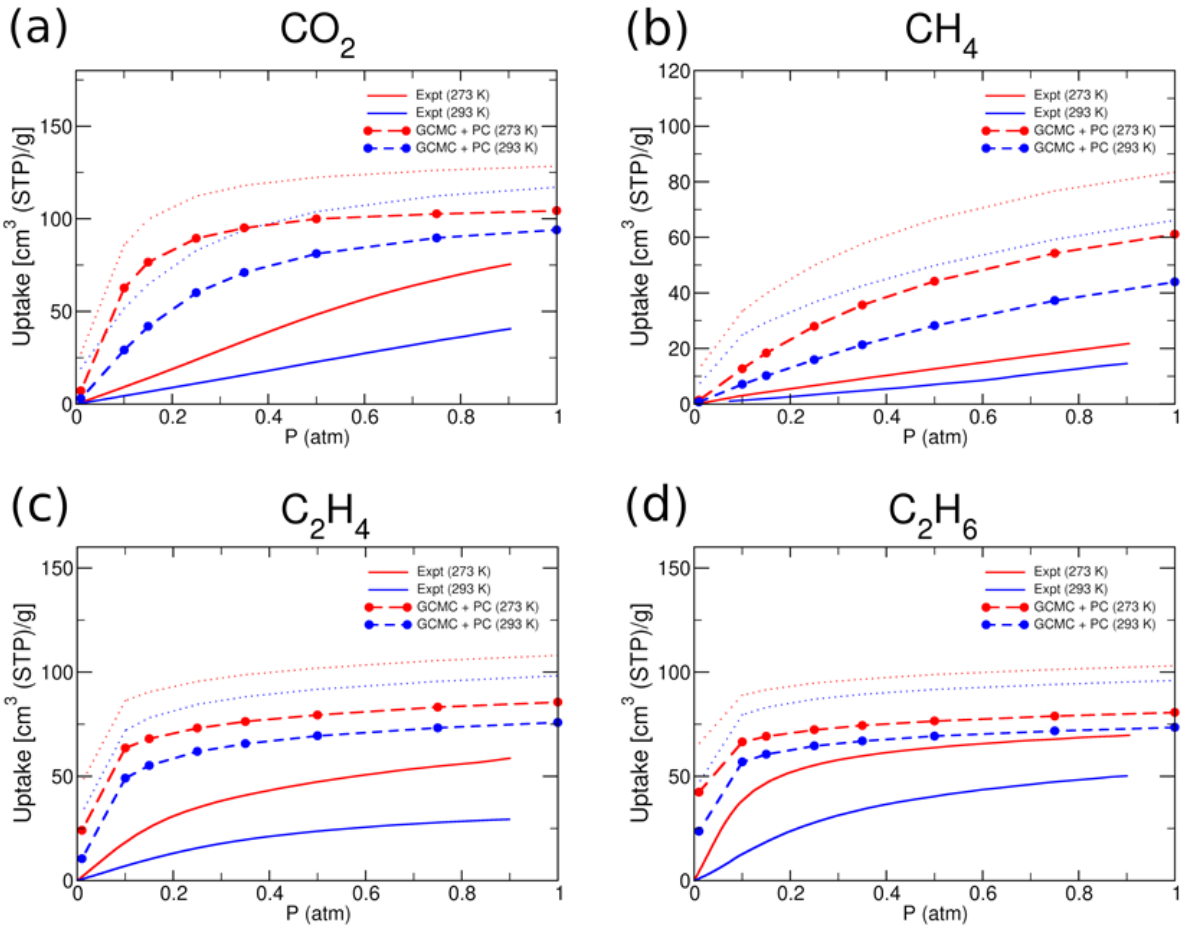

Fig. S41. Comparison of experimentally determined isotherms with those of GCMC predicted isotherms. Solid, dotted, and dashed lines represent experimental, GCMC predicted, and GCMC (with small pore channel blocking) predicted isotherms. Red and blue lines represent isotherms measured/calculated at 273 and 293 K, respectively.

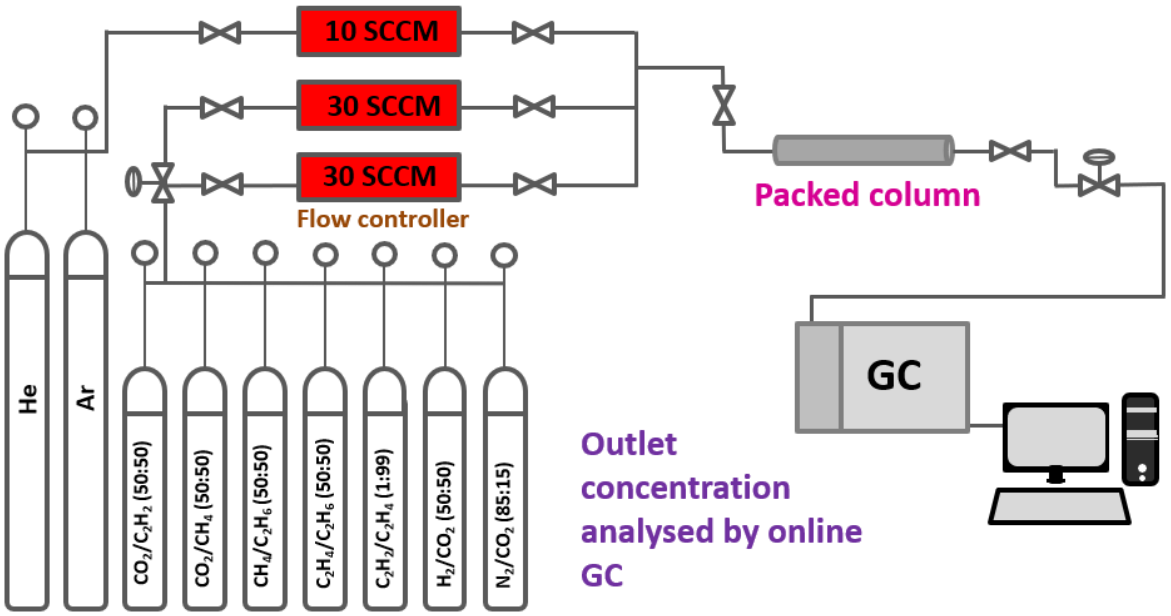

Fig. S42. Schematic representation of custom-made column breakthrough separation arrangement.

Stepwise dynamic breakthrough separation

Stepwise dynamic breakthrough separation (SDBS) minutely differs from usual breakthrough operation as it involves complete desorption of both the gas mixtures from the packed column by making the material regenerated for subsequent experiments with ultrahigh purification of each commodity. The material was first activated prior to loading in the column and further after loading it was further regenerated by continuous flowing of carrier gas for 1 h. The SDBS of the M15 (~1.048 g) for CO_2/CH_4, CH_4/CO_2, C_2H_2/CO_2, C_2H_4/C_2H_6 gas mixtures were analyzed by using packed column of 16.5 cm length and 0.3 cm diameter. The continuous flow was regulated by mass flow controller by using Helium as a carrier gas with a total flow of 2.2-2.9 mL/min (Figure 4). Further breakthrough separation was performed by using quaternary gas mixtures as $C_2H_4/C_2H_6/C_2H_2/CO_2$ (0.25:0.25:0.25:0.25; v/v/v/v) and $C_2H_4/C_2H_6/C_2H_2/CH_4$ (0.75:0.12:0.01:0.12; v/v/v/v). Likewise, He used as a carrier gas contributes 85% of total concentration with a flow of 3.2-3.5 mL/min. The relative percentage of outlet gas was analyzed by gas chromatography (Agilent 7890 B).

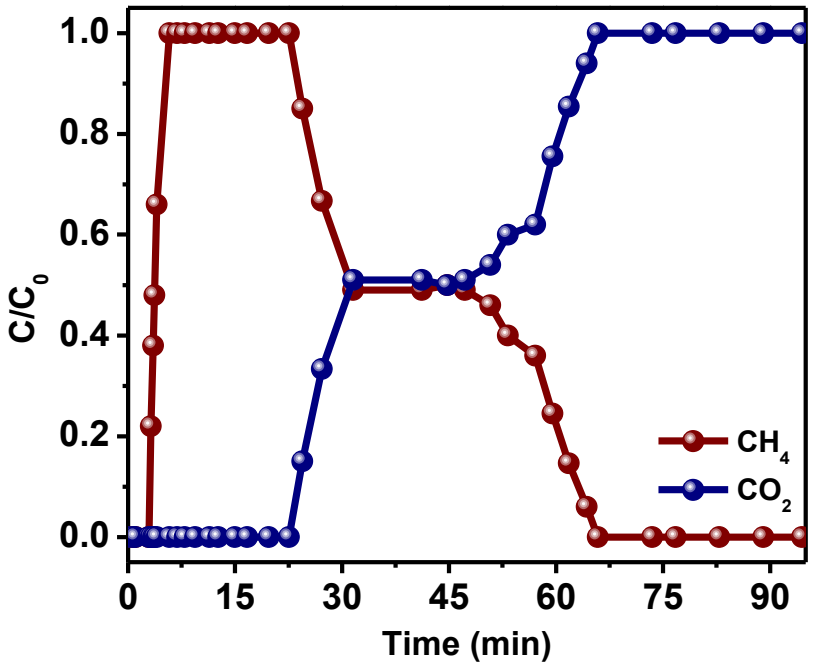

Fig. S43. Experimental column breakthrough curves for equimolar CO_2/CH_4 gas mixtures.

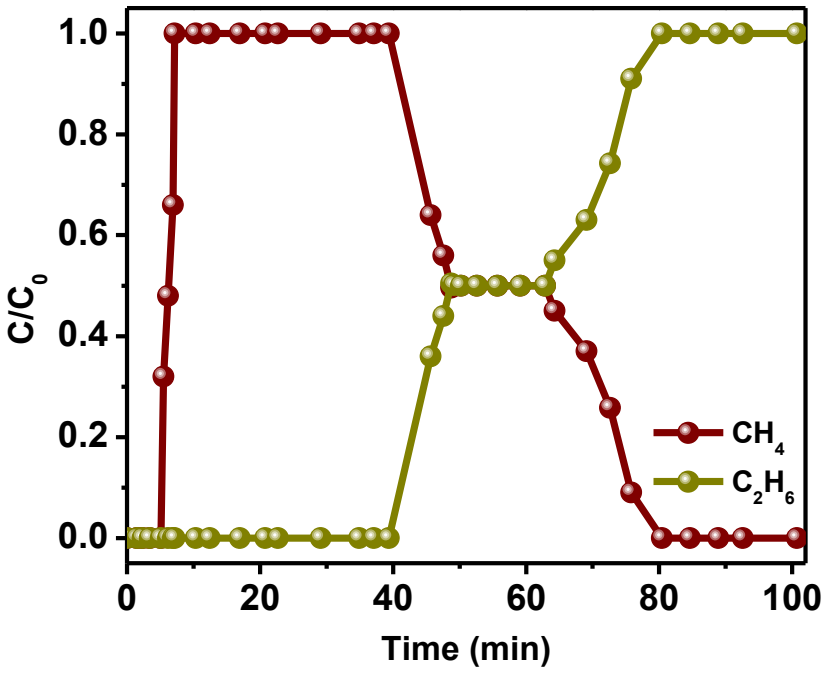

Fig. S44. Experimental column breakthrough curves for equimolar C_2H_6/CH_4 gas mixtures.

Table S6: Summary of the adsorption uptake (mmol/g) and selectivity for C_2H_6 over C_2H_4 in different ethane-selective adsorbents (~ 100 kPa, 293 or 298 K).

Adsorbents	**Uptake ratio % A:B (C_2H_6/C_2H_4)**	**Adsorptive capacity (mmol/g)**		**IAST selectivity**	**Q_{st} (kJ/mol)**		**Ref.**
		A	B		**C_2H_6**	**C_2H_4**	
ZIF-7	101.6	1.83	1.80	1.5	27.3	24.7	33
ZIF-8	132.6	2.03	1.53	1.7	22.2	16.3	34
Ni(bdc)(ted)$_{0.5}$	147.05	5.0	3.4	1.6	21.5	18.3	35
PCN-250	123.22	5.2	4.22	1.9	23.6	21.1	36
UTSA-33	101.47	2.76	2.72	1.4	--	--	37
UTSA-35	112.5	2.43	2.17	1.4	--	--	38
MIL-142A	131.03	3.8	2.9	1.5	27.3	26.2	39
MUF-15	113.01	4.69	4.15	1.96	29.2	28.2	40
CPM-233	114.2	7.45	6.52	1.64	27.3	26.7	41
TJT-100	107.5	4.71	4.38	1.2	29	25	42
IRMOF-8	104.84	5.02	4.79	1.8	52.5	50.5	43
Cu(Qc)$_2$	237.17	1.85	0.78	3.75	29	25.4	44
Ni(TMBDC)(DABCO)$_{0.5}$	143	4.36	3.04	1.98	39	32	45
Azole-Th-1	132.12	4.73	3.58	1.46	28.6	26.1	46

HOF-76a	176.64	2.95	1.67	2	22.8	21	[47]
Al-MOFM$_{15}$	172.42	2.23	1.29	2.51	45.25	33.03	This work

Table S7: Comparison of uptake ratios of C_2H_2 over CO_2 and CH_4 individually in different acetylene-selective adsorbents (~ 100 kPa, 293 or 298 K).

Adsorbent	**Uptake ratio A:B (C_2H_2/CO_2)**	**Adsorptive capacity (mmol/g)**		**Selectivity (50:50)**	**Uptake ratio C:D (C_2H_2/C_2H_4)**	**Adsorptive capacity (mmol/g)**		**Selectivity (50:50)**	**Reference**
		A	B			C	D		
Na-CM	1.01	0.95	0.94	--	1.079	0.95	0.88	7.1	[48]
UiO-66-(COOH)$_2$	1.29	2.32	1.58	2.1	--	2.32	--	--	[49]
JCM-1	1.97	3.34	1.69	4.4	2.14	3.34	1.56	3.1	[50]
HKUST	1.78	8.97	5.03	2.4	1.77	8.97	5.04	2.0	[51]
Mg(HCOO)$_2$	1.47	2.94	2	--	--	2.94	--	--	[52]
UTSA-74-Zn	1.53	4.82	3.16	7.6	--	4.82	--	--	[53]
SIFSIX-1-Cu	1.74	8.5	4.88	--	2.07	8.5	4.11	10.63	[54]
SIFSIX-3-Zn	1.43	3.64	2.54	--	1.62	3.64	2.24	8.82	[54]
MOF-74-Co	--	8.16	--	--	1.16	8.16	7	2.2	[55]

MOF-74-Fe	--	6.8	--	--	1.11	6.8	6.1	2.08	[55]
TJT-100	--	5.37	--	--	1.31	5.37	4.38	--	[42]
NOTT-300	--	6.34	--	--	1.48	6.34	4.28	2.17	[55]
Al-MOFM$_{15}$	1.6	2.85	1.78	2.54	2.2	2.85	1.29	3.32	This work

References

1. Laha, S.; Rambabu, D.; Bhattacharyya, S.; Maji, T. K., Modulating Hierarchical Micro/Mesoporosity by a Mixed Solvent Approach in Al-MOF: Stabilization of MAPbBr3 Quantum Dots. *Chemistry – A European Journal* **2020,** *26* (64), 14671-14678.
2. Yang, L.; Qian, S.; Wang, X.; Cui, X.; Chen, B.; Xing, H., Energy-efficient separation alternatives: metal–organic frameworks and membranes for hydrocarbon separation. *Chemical Society Reviews* **2020,** *49* (15), 5359-5406.
3. Li, J.-R.; Kuppler, R. J.; Zhou, H.-C., Selective gas adsorption and separation in metal–organic frameworks. *Chemical Society Reviews* **2009,** *38* (5), 1477-1504.
4. Nuhnen, A.; Janiak, C., A practical guide to calculate the isosteric heat/enthalpy of adsorption via adsorption isotherms in metal–organic frameworks, MOFs. *Dalton Transactions* **2020,** *49* (30), 10295-10307.
5. Suzuki, M.; Suzuki, M., *Adsorption engineering*. Kodansha Tokyo: 1990; Vol. 14.
6. Yang, R. T., *Gas separation by adsorption processes*. World Scientific: 1997; Vol. 1.
7. Akkermans, R. L. C.; Spenley, N. A.; Robertson, S. H., Monte Carlo methods in Materials Studio. *Molecular Simulation* **2013,** *39* (14-15), 1153-1164.
8. Pincus, M., Letter to the Editor—A Monte Carlo Method for the Approximate Solution of Certain Types of Constrained Optimization Problems. *Operations Research* **1970,** *18* (6), 1225-1228.
9. Comotti, A.; Bracco, S.; Sozzani, P.; Horike, S.; Matsuda, R.; Chen, J.; Takata, M.; Kubota, Y.; Kitagawa, S., Nanochannels of Two Distinct Cross-Sections in a Porous Al-Based Coordination Polymer. *Journal of the American Chemical Society* **2008,** *130* (41), 13664-13672.
10. Rappe, A. K.; Goddard, W. A., Charge equilibration for molecular dynamics simulations. *The Journal of Physical Chemistry* **1991,** *95* (8), 3358-3363.
11. Myers, A. L.; Prausnitz, J. M., Thermodynamics of mixed-gas adsorption. *AIChE Journal* **1965,** *11* (1), 121-127.
12. Kühne, T. D.; Iannuzzi, M.; Del Ben, M.; Rybkin, V. V.; Seewald, P.; Stein, F.; Laino, T.; Khaliullin, R. Z.; Schütt, O.; Schiffmann, F.; Golze, D.; Wilhelm, J.; Chulkov, S.; Bani-Hashemian, M. H.; Weber, V.; Borštnik, U.; Taillefumier, M.; Jakobovits, A. S.; Lazzaro, A.; Pabst, H.; Müller, T.; Schade, R.; Guidon, M.; Andermatt, S.; Holmberg, N.; Schenter, G. K.; Hehn, A.; Bussy, A.; Belleflamme, F.; Tabacchi, G.; Glöß, A.; Lass, M.; Bethune, I.; Mundy, C. J.; Plessl, C.; Watkins, M.; VandeVondele, J.; Krack, M.; Hutter, J.,

CP2K: An electronic structure and molecular dynamics software package - Quickstep: Efficient and accurate electronic structure calculations. *The Journal of Chemical Physics* **2020,** *152* (19), 194103.
13. Hutter, J.; Iannuzzi, M.; Schiffmann, F.; VandeVondele, J., cp2k: atomistic simulations of condensed matter systems. *WIREs Computational Molecular Science* **2014,** *4* (1), 15-25.
14. VandeVondele, J.; Krack, M.; Mohamed, F.; Parrinello, M.; Chassaing, T.; Hutter, J., Quickstep: Fast and accurate density functional calculations using a mixed Gaussian and plane waves approach. *Computer Physics Communications* **2005,** *167* (2), 103-128.
15. Perdew, J. P.; Burke, K.; Ernzerhof, M., Generalized Gradient Approximation Made Simple. *Physical Review Letters* **1996,** *77* (18), 3865-3868.
16. Grimme, S.; Antony, J.; Ehrlich, S.; Krieg, H., A consistent and accurate ab initio parametrization of density functional dispersion correction (DFT-D) for the 94 elements H-Pu. *The Journal of Chemical Physics* **2010,** *132* (15), 154104.
17. Grimme, S.; Ehrlich, S.; Goerigk, L., Effect of the damping function in dispersion corrected density functional theory. *Journal of Computational Chemistry* **2011,** *32* (7), 1456-1465.
18. Goedecker, S.; Teter, M.; Hutter, J., Separable dual-space Gaussian pseudopotentials. *Physical Review B* **1996,** *54* (3), 1703-1710.
19. Hartwigsen, C.; Goedecker, S.; Hutter, J., Relativistic separable dual-space Gaussian pseudopotentials from H to Rn. *Physical Review B* **1998,** *58* (7), 3641-3662.
20. Krack, M., Pseudopotentials for H to Kr optimized for gradient-corrected exchange-correlation functionals. *Theoretical Chemistry Accounts* **2005,** *114* (1), 145-152.
21. VandeVondele, J.; Hutter, J., Gaussian basis sets for accurate calculations on molecular systems in gas and condensed phases. *The Journal of Chemical Physics* **2007,** *127* (11), 114105.
22. Bussi, G.; Donadio, D.; Parrinello, M., Canonical sampling through velocity rescaling. *The Journal of Chemical Physics* **2007,** *126* (1), 014101.
23. Dubbeldam, D.; Calero, S.; Ellis, D. E.; Snurr, R. Q., RASPA: molecular simulation software for adsorption and diffusion in flexible nanoporous materials. *Molecular Simulation* **2016,** *42* (2), 81-101.
24. Dubbeldam, D.; Torres-Knoop, A.; Walton, K. S., On the inner workings of Monte Carlo codes. *Molecular Simulation* **2013,** *39* (14-15), 1253-1292.
25. Dubbeldam, D.; Snurr, R. Q., Recent developments in the molecular modeling of diffusion in nanoporous materials. *Molecular Simulation* **2007,** *33* (4-5), 305-325.
26. Rappe, A. K.; Casewit, C. J.; Colwell, K. S.; Goddard, W. A.; Skiff, W. M., UFF, a full periodic table force field for molecular mechanics and molecular dynamics simulations. *Journal of the American Chemical Society* **1992,** *114* (25), 10024-10035.
27. Limas, N. G.; Manz, T. A., Introducing DDEC6 atomic population analysis: part 4. Efficient parallel computation of net atomic charges, atomic spin moments, bond orders, and more. *RSC Advances* **2018,** *8* (5), 2678-2707.
28. Martin, M. G.; Siepmann, J. I., Transferable Potentials for Phase Equilibria. 1. United-Atom Description of n-Alkanes. *The Journal of Physical Chemistry B* **1998,** *102* (14), 2569-2577.
29. Wick, C. D.; Martin, M. G.; Siepmann, J. I., Transferable Potentials for Phase Equilibria. 4. United-Atom Description of Linear and Branched Alkenes and Alkylbenzenes. *The Journal of Physical Chemistry B* **2000,** *104* (33), 8008-8016.
30. Potoff, J. J.; Siepmann, J. I., Vapor–liquid equilibria of mixtures containing alkanes, carbon dioxide, and nitrogen. *AIChE Journal* **2001,** *47* (7), 1676-1682.

31. Shah, M. S.; Siepmann, J. I.; Tsapatsis, M., Transferable potentials for phase equilibria. Improved united-atom description of ethane and ethylene. *AIChE Journal* **2017,** *63* (11), 5098-5110.
32. Eggimann, B. L.; Sun, Y.; DeJaco, R. F.; Singh, R.; Ahsan, M.; Josephson, T. R.; Siepmann, J. I., Assessing the Quality of Molecular Simulations for Vapor–Liquid Equilibria: An Analysis of the TraPPE Database. *Journal of Chemical & Engineering Data* **2020,** *65* (3), 1330-1344.
33. Gücüyener, C.; van den Bergh, J.; Gascon, J.; Kapteijn, F., Ethane/Ethene Separation Turned on Its Head: Selective Ethane Adsorption on the Metal−Organic Framework ZIF-7 through a Gate-Opening Mechanism. *Journal of the American Chemical Society* **2010,** *132* (50), 17704-17706.
34. Böhme, U.; Barth, B.; Paula, C.; Kuhnt, A.; Schwieger, W.; Mundstock, A.; Caro, J.; Hartmann, M., Ethene/Ethane and Propene/Propane Separation via the Olefin and Paraffin Selective Metal–Organic Framework Adsorbents CPO-27 and ZIF-8. *Langmuir* **2013,** *29* (27), 8592-8600.
35. Liang, W.; Xu, F.; Zhou, X.; Xiao, J.; Xia, Q.; Li, Y.; Li, Z., Ethane selective adsorbent Ni(bdc)(ted)0.5 with high uptake and its significance in adsorption separation of ethane and ethylene. *Chemical Engineering Science* **2016,** *148*, 275-281.
36. Chen, Y.; Qiao, Z.; Wu, H.; Lv, D.; Shi, R.; Xia, Q.; Zhou, J.; Li, Z., An ethane-trapping MOF PCN-250 for highly selective adsorption of ethane over ethylene. *Chemical Engineering Science* **2018,** *175*, 110-117.
37. He, Y.; Zhang, Z.; Xiang, S.; Fronczek, F. R.; Krishna, R.; Chen, B., A Microporous Metal–Organic Framework for Highly Selective Separation of Acetylene, Ethylene, and Ethane from Methane at Room Temperature. *Chemistry – A European Journal* **2012,** *18* (2), 613-619.
38. He, Y.; Zhang, Z.; Xiang, S.; Fronczek, F. R.; Krishna, R.; Chen, B., A robust doubly interpenetrated metal–organic framework constructed from a novel aromatic tricarboxylate for highly selective separation of small hydrocarbons. *Chemical Communications* **2012,** *48* (52), 6493-6495.
39. Chen, Y.; Wu, H.; Lv, D.; Shi, R.; Chen, Y.; Xia, Q.; Li, Z., Highly Adsorptive Separation of Ethane/Ethylene by An Ethane-Selective MOF MIL-142A. *Industrial & Engineering Chemistry Research* **2018,** *57* (11), 4063-4069.
40. Qazvini, O. T.; Babarao, R.; Shi, Z.-L.; Zhang, Y.-B.; Telfer, S. G., A Robust Ethane-Trapping Metal–Organic Framework with a High Capacity for Ethylene Purification. *Journal of the American Chemical Society* **2019,** *141* (12), 5014-5020.
41. Yang, H.; Wang, Y.; Krishna, R.; Jia, X.; Wang, Y.; Hong, A. N.; Dang, C.; Castillo, H. E.; Bu, X.; Feng, P., Pore-Space-Partition-Enabled Exceptional Ethane Uptake and Ethane-Selective Ethane–Ethylene Separation. *Journal of the American Chemical Society* **2020,** *142* (5), 2222-2227.
42. Hao, H.-G.; Zhao, Y.-F.; Chen, D.-M.; Yu, J.-M.; Tan, K.; Ma, S.; Chabal, Y.; Zhang, Z.-M.; Dou, J.-M.; Xiao, Z.-H.; Day, G.; Zhou, H.-C.; Lu, T.-B., Simultaneous Trapping of C2H2 and C2H6 from a Ternary Mixture of C2H2/C2H4/C2H6 in a Robust Metal–Organic Framework for the Purification of C2H4. *Angewandte Chemie International Edition* **2018,** *57* (49), 16067-16071.
43. Liao, P.-Q.; Zhang, W.-X.; Zhang, J.-P.; Chen, X.-M., Efficient purification of ethene by an ethane-trapping metal-organic framework. *Nature Communications* **2015,** *6* (1), 8697.
44. Lin, R.-B.; Wu, H.; Li, L.; Tang, X.-L.; Li, Z.; Gao, J.; Cui, H.; Zhou, W.; Chen, B., Boosting Ethane/Ethylene Separation within Isoreticular Ultramicroporous Metal–Organic Frameworks. *Journal of the American Chemical Society* **2018,** *140* (40), 12940-12946.
45. Wang, X.; Niu, Z.; Al-Enizi, A. M.; Nafady, A.; Wu, Y.; Aguila, B.; Verma, G.; Wojtas, L.; Chen, Y.-S.; Li, Z.; Ma, S., Pore environment engineering in metal–organic

frameworks for efficient ethane/ethylene separation. *Journal of Materials Chemistry A* **2019,** *7* (22), 13585-13590.
46. Xu, Z.; Xiong, X.; Xiong, J.; Krishna, R.; Li, L.; Fan, Y.; Luo, F.; Chen, B., A robust Th-azole framework for highly efficient purification of C2H4 from a C2H4/C2H2/C2H6 mixture. *Nature Communications* **2020,** *11* (1), 3163.
47. Zhang, X.; Li, L.; Wang, J.-X.; Wen, H.-M.; Krishna, R.; Wu, H.; Zhou, W.; Chen, Z.-N.; Li, B.; Qian, G.; Chen, B., Selective Ethane/Ethylene Separation in a Robust Microporous Hydrogen-Bonded Organic Framework. *Journal of the American Chemical Society* **2020,** *142* (1), 633-640.
48. Wang, J.; Zhu, Q.; Zhang, Z.; Sadakane, M.; Li, Y.; Ueda, W., Zeolitic Octahedral Metal Oxides with Ultra-Small Micropores for C2 Hydrocarbon Separation. *Angewandte Chemie International Edition* **2021,** *60* (33), 18328-18334.
49. Zhang, L.; Jiang, K.; Yang, L.; Li, L.; Hu, E.; Yang, L.; Shao, K.; Xing, H.; Cui, Y.; Yang, Y.; Li, B.; Chen, B.; Qian, G., Benchmark C2H2/CO2 Separation in an Ultra-Microporous Metal–Organic Framework via Copper(I)-Alkynyl Chemistry. *Angewandte Chemie International Edition* **2021,** *60* (29), 15995-16002.
50. Lee, J.; Chuah, C. Y.; Kim, J.; Kim, Y.; Ko, N.; Seo, Y.; Kim, K.; Bae, T. H.; Lee, E., Separation of Acetylene from Carbon Dioxide and Ethylene by a Water-Stable Microporous Metal–Organic Framework with Aligned Imidazolium Groups inside the Channels. *Angewandte Chemie International Edition* **2018,** *57* (26), 7869-7873.
51. Fischer, M.; Hoffmann, F.; Fröba, M., New Microporous Materials for Acetylene Storage and C2H2/CO2 Separation: Insights from Molecular Simulations. *ChemPhysChem* **2010,** *11* (10), 2220-2229.
52. Kim, H.; Samsonenko, D. G.; Yoon, M.; Yoon, J. W.; Hwang, Y. K.; Chang, J.-S.; Kim, K., Temperature-triggered gate opening for gas adsorption in microporous manganese formate. *Chemical Communications* **2008,** (39), 4697-4699.
53. Luo, F.; Yan, C.; Dang, L.; Krishna, R.; Zhou, W.; Wu, H.; Dong, X.; Han, Y.; Hu, T.-L.; O'Keeffe, M.; Wang, L.; Luo, M.; Lin, R.-B.; Chen, B., UTSA-74: A MOF-74 Isomer with Two Accessible Binding Sites per Metal Center for Highly Selective Gas Separation. *Journal of the American Chemical Society* **2016,** *138* (17), 5678-5684.
54. Cui, X.; Chen, K.; Xing, H.; Yang, Q.; Krishna, R.; Bao, Z.; Wu, H.; Zhou, W.; Dong, X.; Han, Y.; Li, B.; Ren, Q.; Zaworotko Michael, J.; Chen, B., Pore chemistry and size control in hybrid porous materials for acetylene capture from ethylene. *Science* **2016,** *353* (6295), 141-144.
55. Hu, T.-L.; Wang, H.; Li, B.; Krishna, R.; Wu, H.; Zhou, W.; Zhao, Y.; Han, Y.; Wang, X.; Zhu, W.; Yao, Z.; Xiang, S.; Chen, B., Microporous metal–organic framework with dual functionalities for highly efficient removal of acetylene from ethylene/acetylene mixtures. *Nature Communications* **2015,** *6* (1), 7328.